7-11-2022

# Predictive Thermal Modeling and Characterization of Ultrasonic Consolidation Process for Thermoplastic Composites

Madeline Kirby
*Louisiana State University and Agricultural and Mechanical College*

# PREDICTIVE THERMAL MODELING AND CHARACTERIZATION OF ULTRASONIC CONSOLIDATION PROCESS FOR THERMOPLASTIC COMPOSITES

A Thesis

Submitted to the Graduate Faculty of
the Louisiana State University
Agricultural and Mechanical College
in partial fulfillment of the
requirements for the degree of
Master of Science

in

The Department of Mechanical
Engineering

by
Madeline Kirby
B.S., Louisiana State University, 2021
August 2022

## ACKNOWLEDGEMENTS

Foremost, I would like to acknowledge my faculty advisor Dr. Genevieve Palardy for her invaluable guidance, patience, and trust throughout my studies. She never hesitated to help with anything I asked, and her confidence in my abilities drove me to become a better researcher, presenter, leader, and engineer. I would also like to thank Dr. Guoqiang Li and Dr. Manas Gartia for agreeing to serve on my advisory committee as well as Dr. Michelle Osborne from the LSU School of Veterinary Medicine, for her assistance with μCT scans. Next, I would like to thank all my family, friends, and professors who have relentlessly cheered me on throughout my entire academic journey and pushed me to pursue a graduate education. To my father Klein, an absolute tour-de-force of an engineer and knower of all things mechanical, thank you for cultivating this passion in me and for being my biggest role model and inspiration. To my mother Dana, a person who is paradoxically the most tenacious and most gentle I have ever known, thank you for showing me that brilliant, empathetic, industrious women who think deeply and love unequivocally can also be some of the best engineers on the planet. To my partner Cade, thank you for loving me, for always being my rock, for having patience during this intense period of study, and for pushing me to work for those '10 more minutes' for so many late nights. Finally, thank you to the National Science Foundation and the Louisiana Board of Regents for providing the funding that made this research possible.

## TABLE OF CONTENTS

## LIST OF TABLES

## LIST OF FIGURES

## ABSTRACT

Ultrasonic consolidation (USC) of thermoplastic composites (TPCs) is a highly attractive and promising method to manufacture high-performance composites. This work focuses on USC of dry carbon fiber (CF) fabrics with high-temperature polyphenylene sulfide (PPS) films. Experimental trials to assess feasibility of the process are time-consuming. Consequently, a predictive thermal model would facilitate process parameters selection to reduce expensive trial-and-error approaches. This paper presents a 2D finite element model of samples under consolidation, incorporating equations for viscoelastic heating, matrix phase change, and material properties. Theoretical temperature profiles for nodes of interest were compared to the corresponding experimental temperature curves for various control parameters (i.e., weld time and vertical displacement of sonotrode) and showed good agreement during heating phase. It was found that welding time values below 1500 ms were insufficient to reach melting temperature, whereas weld times above 3000 ms led to the lowest average void content (2.43 ± 0.81 %). More specifically, the time the material spent above melting temperature, i.e., residence time, was established as a parameter that could estimate cases resulting in better consolidation and lower void content (time above 2600 ms for void content below 2.5 %). Overall, the thermal model and micro-structural outcomes confirmed the feasibility of the USC process for layered composites made from dry fabric and high-temperature thermoplastic films.

# 1. INTRODUCTION

## 1.1. Motivation and Purpose

The modern expansion and technological evolution of the aerospace and automotive industries has increased the demand for high-quality and cost-effective manufacturing processes for lightweight composite structures. TPCs are highly compatible with this demand, as they require shorter manufacturing times than traditional thermoset composites and can be re-heated for molding and forming, as well as assembled through fusion bonding (i.e., welding) [1]. USC of TPCs is a promising high-speed manufacturing method, providing energy efficiency and ease of automation. It utilizes ultrasonic vibrations and pressure applied by a horn (or sonotrode) to generate frictional and viscoelastic heating between material layers, thereby melting the thermoplastic matrix and infusing the fibers to produce semi-finished parts. So far, its feasibility has been demonstrated for consolidation of TPC prepregs, rovings, and dry fibers.

## 1.2. Research Objectives

This study focuses on USC of dry CF fabric layers with high-temperature PPS films. While previous work demonstrated feasibility of this process under a range of welding forces [2], experimental trials are time-consuming. Consequently, a predictive thermal model would facilitate process parameters selection to reduce expensive trial-and-error campaigns. This paper's main goal is two-fold: 1) develop a simplified FE model to predict temperature profile for CF/PPS samples with experimental validation; and 2) further understand the effect of ultrasonic control parameters (vertical sonotrode

displacement or weld time) on micro-structural quality to provide process guidelines based on thermal history.

### 1.3. Thesis Outline

This thesis will first present the implementation of a predictive 2D FE model for the cross-sectional temperature distribution of samples under consolidation, using the MATLAB PDE solver. Theoretical temperature profiles for various welding parameters are then compared to the corresponding experimental temperature values to assess the model's accuracy. Finally, consolidated samples are characterized for void content through micro-Computed Tomography ($\mu$CT) and optical microscopy.

# 2. LITERATURE REVIEW

This chapter will review the contents of existing literature pertaining to the fabrication of continuous fiber reinforced TPCs, process modeling for USC, and characterization of ultrasonically consolidated TPCs. Traditional and advanced manufacturing techniques for fiber reinforced TPCs will be explained. Then, studies relating to the modeling of the USC process for different manufacturing setups will be discussed. Lastly, existing methods of thermal, microstructural, and mechanical characterization of composite samples will be explored.

## 2.1. Fabrication of Fiber Reinforced Thermoplastic Composites

Fiber-reinforced TPCs are comprised of high tensile strength fibers, such as glass fiber (GF) or carbon fiber (CF), that reinforce a thermoplastic polymer matrix. The latter ranges from low temperature thermoplastics, such as polypropylene (PP), to high temperature thermoplastics, such as polyphenylene sulfide (PPS), polyetherimide (PEI), poly ether ether ketone (PEEK), or poly ether ketone ketone (PEKK) [3]. Although there are several methods conventionally used to create these composites on an industrial scale, there are emerging processes such as USC that aim to decrease turnaround time, power consumption, and material waste at lower fabrication costs [4, 5].

### 2.1.1. Traditional Manufacturing Methods

There are three primary mechanisms utilized in traditional TPC manufacturing: filament winding, molding, and forming. Filament winding, also called tape winding, is a process in which thermoplastic prepreg (pre-impregnated) filament is woven over a mandrel, as shown in Figure 2.1. In this method, consolidation occurs at the contact point between the roller and the mandrel through the application of pressure and heat. For this

process, the parameters with the most significant impact on part quality are heat intensity, winding speed, and consolidation force. Filament winding is generally used and preferred for axisymmetric geometries such as pipes or pressure vessels, since it does not require interruption or post-processing [6].

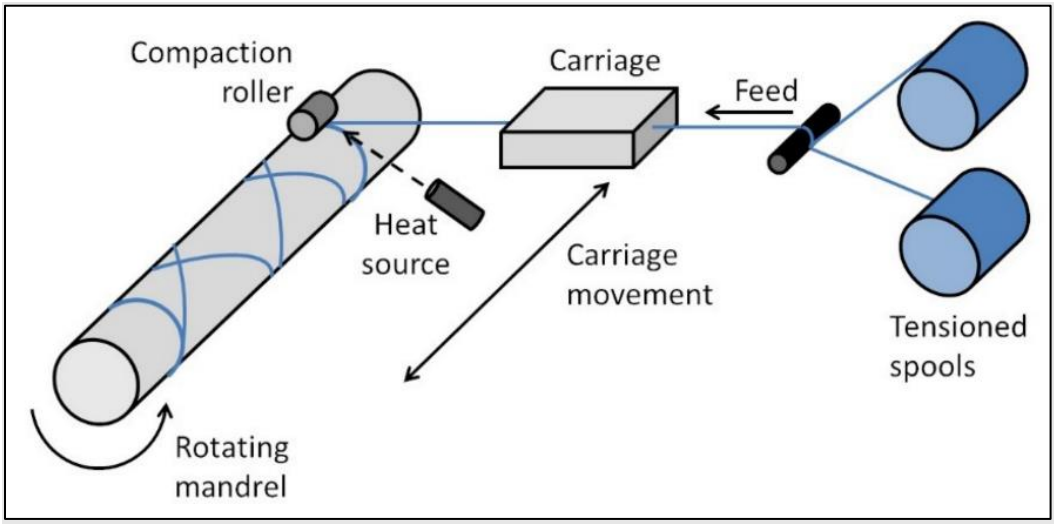


Figure 2.1. Schematic of a filament winding process for TPCs [7].

Compression molding is a process that applies pressure to a thermoplastic part using male and female heated plates to create a finished part, as shown in Figure 2.2. This method has been used to create both flat laminates and parts with certain curved geometries (stamp forming, as shown in Figure 2.3), and can be used on composites with unidirectional fibers, woven fabrics, or randomly oriented fiber materials, in prepreg or strand form [8, 9].

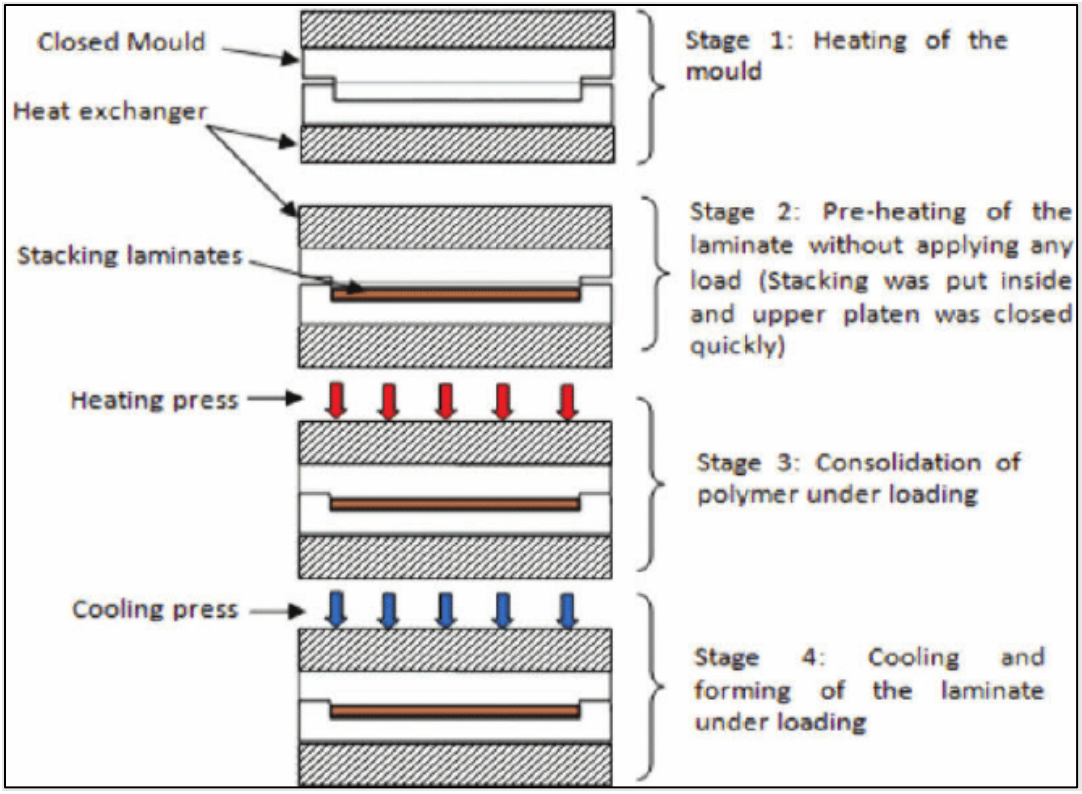


Figure 2.2. Schematic diagram of a compression molding process used to fabricate composite laminates [10].

Stamp forming is a process used for the rapid production of structural composites at low cost (shown in Figure 2.3). In general, a stamp forming process starts with preheating the material before transferring it to a matched metal tool set (die set). The two halves are brought together and apply a designated pressure to the heated material and form it into the shape of the mold. After a certain holding time, the halves are separated, and the part is removed from the mold. For TPCs, this technology has not seen its full potential at a large scale due to low production volumes, high equipment and tooling costs and presence of fiber distortion in the completed part [12].

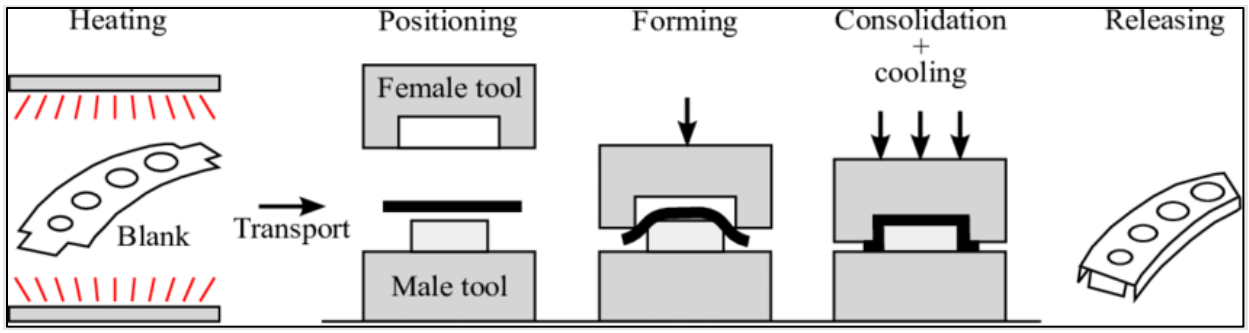

Figure 2.3. Schematic of a stamp forming process for a composite material [11].

A study conducted by Brooks et al. [13] investigated the shortcomings associated with stamp forming continuous fiber TPCs, providing recommendations for the reduction of the primary defects (i.e. fiber wrinkling, voids) associated with the process. They assessed the advantages and disadvantages associated with processing temperature, forming speed, applied pressure, holding time, and cooling rate. While results were generally inconclusive regarding ideal parameter ranges, the authors suggest that optimization of these parameters may be possible with a systematic study of the material.

Autoclave forming of TPCs is a technique that can be used to consolidate fibers and matrix or re-shape pre-consolidated laminates. Autoclaves utilize air pressure to form the composite material into the geometry of a female mold in a sealed chamber [15]. While this process is widely used in industry for thermoset composites, thermoplastics pose an additional challenge since high-temperature process conditions are required. Fernández et al. conducted a study wherein a standard autoclave was adapted for high-temperature TPC processing and showed that the fabrication of complex parts based on existing aeronautical substructures was viable [16]. However, alternative out-of-autoclave fabrication methods are often investigated due to the high energy consumption required by autoclave production.

Much like compression molding, injection molding also requires a mold comprised of male and female shells. Dry fibers are placed into the mold and sealed between the two halves before molten thermoplastic resin is injected into the cavity [14]. Once the thermoplastic is cooled, the finished part can be removed from the mold.

### 2.1.2. Advanced Manufacturing Methods

Some other advanced manufacturing processes are being researched to address the shortcomings of traditional methods. Automated fiber placement (AFP) is an automated layup method wherein a robotic system can precisely lay fibers in a desired orientation and press them into place using a heated roller. This method relies on control software to dictate parameters such as tape laying speed, compaction force, and heating temperature. Software is also used to analyze fiber direction and perform simulations to avoid collision of the robotic arm with its surroundings. As such, these processes are often optimized and minimize material waste as a result [17].

While AFP technology is generally used for smaller designs (less than 0.5 m x 0.5 m x 0.5m), automated tape layup (ATL) can be used to fabricate larger parts by covering more surface area with wider tapes (Figure 2.4). AFP technology with thermoset materials has already been introduced in industrial production; however, AFP of TPCs is still in development due to the added requirement of elevated temperatures during processing [18]. The main heating sources for AFP of thermoplastics are infrared, laser, hot gas torch, and ultrasonic vibrations. As an industry example, Dutch aerospace manufacturer GKN Fokker uses AFP systems developed by Macedonian automated solutions company Mikrosam to fabricate TPC aircraft components. The technology utilizes bi-directional placement on both open and closed 3D geometries with a modular head exchange

system that allows for multi-tow AFP or ATP, providing additional user flexibility and manufacturing capability [19].

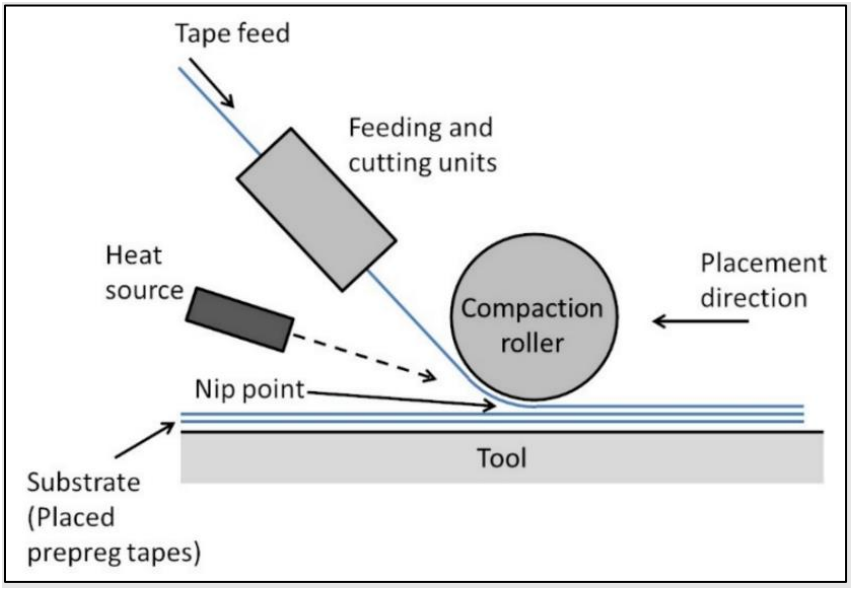


Figure 2.4. Schematic of ATL process with in-situ consolidation for prepreg composite tapes [7].

Fused deposition modeling (FDM) of TPCs uses three-dimensional (3D) computer-aided design (CAD) by stacking the fibers and matrix material in a layered arrangement (Figure 2.5). This layer-based method allows the user to create complex geometries in a short amount of time with minimal human interference [20]. While this method can be quick and cost-effective, the layer-by-layer fabrication method introduces porosity and may reduce the mechanical performance of the part as a result. Dickson et al. studied fused filament fabrication (FFF) to address the inferior mechanical properties that result from traditional composite printing as compared to industry-standard technologies like compression molding. They investigated both short and continuous fiber reinforced materials and found that the maximum achievable mechanical performance was limited due to the inherent porosity of 3D printed parts. To mitigate this issue, the authors suggest

applying pressure while printing, overlapping the fiber bundles, and printing in low-pressure conditions [21].

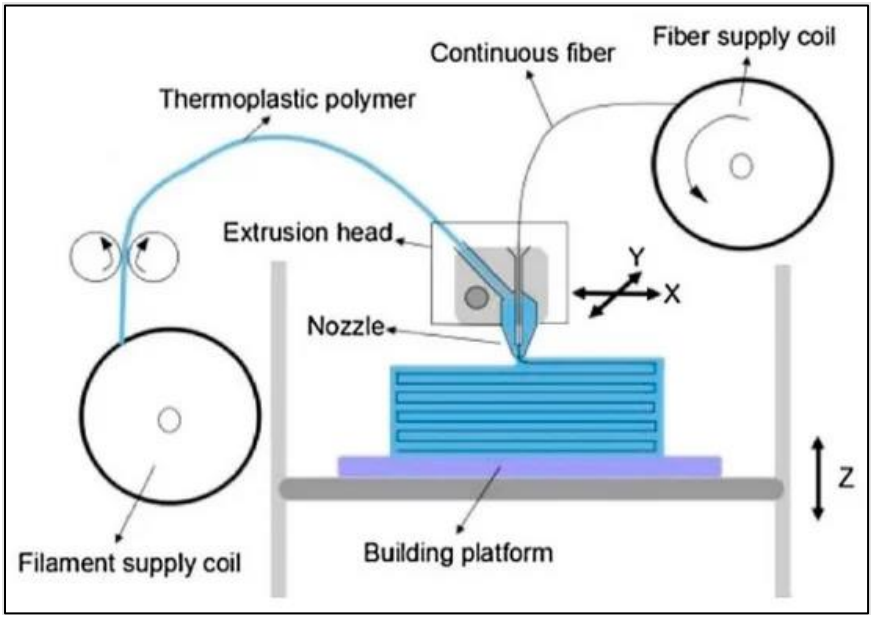


Figure 2.5. Schematic of a FDM process for thermoplastic composite material [20].

Fiber™ is a composite 3D printer created by Desktop Metal [22] that uses micro-automated fiber placement (μAFP) to print industrial-grade parts with exceptionally high resolution and low porosity. The printer utilizes closed-loop heat control to deposit continuous fiber reinforcements with CF or GF tapes within three thermoplastic families: Nylon (PA6), PEEK, and PEKK. The default continuous fiber printhead can also be exchanged for a printhead that extrudes chopped carbon fiber or fiberglass filament. This printer can accommodate most small-scale parts with a maximum build volume of 310 x 240 x 270 mm.

On a larger scale, AREVO's AQUA system [23] is currently the largest continuous carbon fiber 3D printer in the industry. With an approximate build volume of 1000 x 1000 x 1000 mm, AQUA's continuous filament deposition head is mounted on a six-axis robot

that utilizes laser heating and in-situ roller compaction. They currently offer Nylon/CF and produce parts with < 1 % void content.

### 2.1.3. Ultrasonic Consolidation

Traditionally, USC has been used as an additive manufacturing technique used on metal tapes or films called ultrasonic additive manufacturing (UAM) (Figure 2.6). This process applies vibration continuously to weld foil layers together as they are passed under the rolling sonotrode, building the part layer by layer [24]. This is often used in combination with Computer Numerical Control (CNC) to remove material and form the component shape during the build-up process [25].

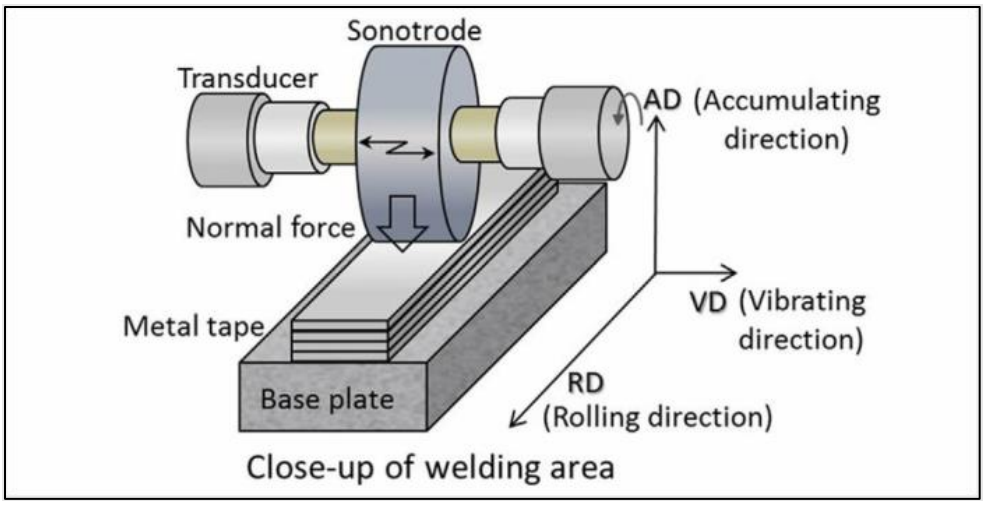


Figure 2.6. Schematic of traditional UAM process used on metal tapes [24].

USC of TPCs is a promising high-speed manufacturing method, providing energy efficiency and ease of automation [2, 26-29]. It utilizes ultrasonic vibrations and pressure applied by a horn (or sonotrode) to generate frictional and viscoelastic heating between material layers, thereby melting the thermoplastic matrix and infusing the fibers to produce semi-finished parts (Figure 2.7). So far, its feasibility has been demonstrated for consolidation of TPC prepregs, rovings, and dry fibers. While the analogous process of

ultrasonic welding (USW) has been utilized since the 1980's [1], research as it pertains to thermoplastic composite parts has only been conducted in depth for just under a decade. This includes experimental studies on weld quality and failure modes in spot welds for short fiber composites [30], process monitoring through output data [31], liquid TPCs joining [32], as well as continuous welding for long seams [33, 34]. More recently, ultrasonic vibrations are also being used as the heating mechanism for filament winding and ATL [26, 35].

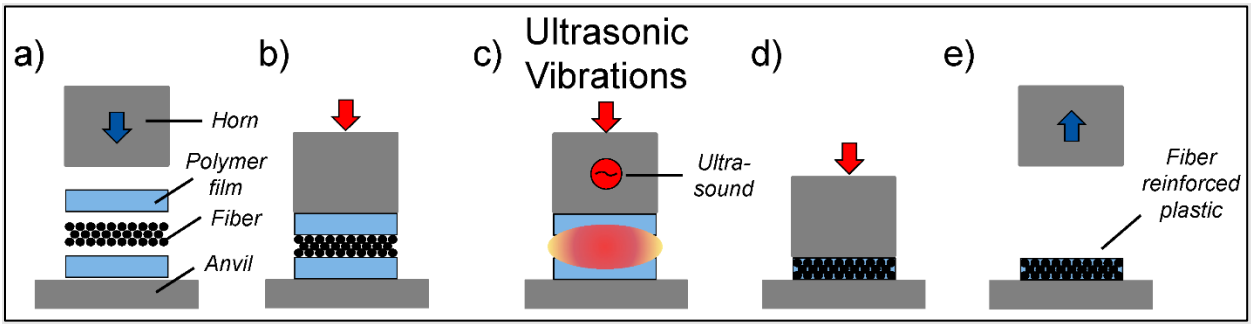


Figure 2.7. Schematic illustration of USC process for CF reinforced composites [29].

Gomer et al. [28] conducted an extensive study on USC of dry CF and GF with polyamide 6 (PA6), polyethylene (PE), and polypropylene (PP) films. They successfully demonstrated the feasibility of this method by stacking thermoplastic film and dry fiber layers, then applying ultrasonic vibrations in a single spot or continuously through a rolling sonotrode. They reported tensile strengths up to 1.2 GPa and a maximum fiber volume fraction of 33 % for CF/PA6 samples. While multiple combinations of materials were experimentally studied, several characteristics were not yet investigated in detail, including micro-structural quality, porosity, heat generation, and matrix crystallization behavior. The authors conclude that while USC of polymer films and fibers is a promising manufacturing method, it should be possible to optimize process parameters to avoid excessive trial-and-error campaigns [29].

Lionetto et al. [11, 12] demonstrated the use of USC for commingled rovings (GF and PP filaments) on a rotating mandrel. The process produced samples with density and storage shear modulus values falling within typical range for compression molded samples. However, the void content (1.9 – 4.6 %) was slightly higher than compression molded samples (1.8 %) .

Rizzolo and Walczyk tested the use of ultrasonic heating for automated fiber placement (AFP) of unidirectional (UD) glass fiber (GF)/high-density polyethylene (HDPE) and UD carbon fiber (CF)/polyethylene terephthalate (PET) tapes [28]. Their aim was to replace traditional AFP heating methods, such as hot gas, infrared, and laser heating. They accomplished this by placing tapes onto a moving stage under a stationary sonotrode, and by manufacturing UD and quasi-isotropic layups. They demonstrated that the strength and stiffness of the layups was lower than compression molded laminates, except for CF/PET.

Dell'Anna et al. expanded upon their previous work by investigating USC of semi-preg UD GF/LPET (poly (ethylene terephthalate)) tapes through physical, mechanical and micro-structural characterization for various winding speeds [36]. Winding speed did not present any clear trend for density, void content (1.7 – 3.2 %), or storage shear modulus, but nonetheless, the reliability of this manufacturing method was demonstrated for this type of UD tape.

### 2.2. Process Modeling for Ultrasonic Consolidation

Due to the trial-and-error nature of investigating consolidation parameters, it is desirable to find a reasonable experimental range to avoid unnecessary expenses or wasted time. Process modeling allows for the prediction of heating phenomena and can

be used to strategically reduce experimental scope. While thermal models exist for similar techniques such as USW and continuous USC, there are few studies on models for stationary sonotrode USC. Thus, these models can be used to inform a new thermal model created specifically for stationary sonotrode USC.

### 2.2.1. Ultrasonic Welding

Although USW is a joining technique, the mechanisms responsible for the melting and joining of composite components are the same for those created through USC. Therefore, it is worthwhile to investigate thermal models that have already been developed for ultrasonic welding processes. In fact, the apparatus used for ultrasonic welding is the same setup as the stationary sonotrode USC used for this study. Numerical studies to predict heat generation have been performed to investigate contact behavior at the interface [7] and to assess temperature rise through a multi-timescale framework [8]. However, those studies are related to the welding process between pre-fabricated adherends, and there have been very few studies on USC of TPCs from raw materials to finished parts.

Levy et al. [37] created a numerical model of the ultrasonic welding of TPCs with flat energy directors to simulate the mechanics, heat transfer, and degree of adhesion throughout the process. The model considers the primary mechanisms involved during the heating phase: the elastic problem produced by mechanical vibrations, the heat transfer problem that predicts the change in temperature, and a coupled bonding evolution problem that predicts the degree of adhesion of the specimens.

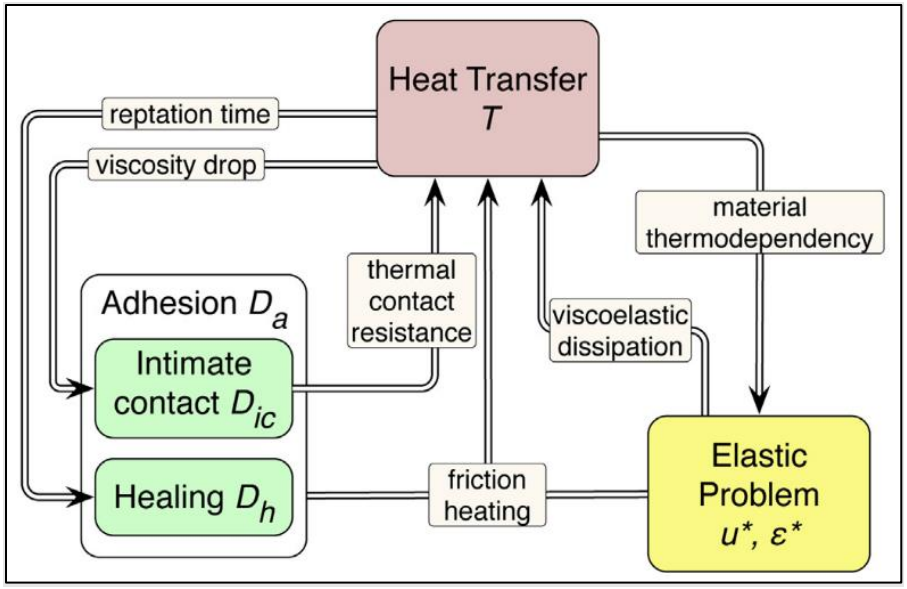


Figure 2.8. Flow diagram of mechanisms involved in heat transfer and their couplings proposed by Levy et al. [37].

CF/PEI samples were welded with PEI films in experimental trials intended to replicate the results of those found by Villegas et al. It was found that the viscoelastic heating was the dominant source of energy dissipation past the initial heating stage with an assumed efficiency of 13 % (Figure 2.9). In this model, additional assumptions were made: i) the adherends were considered isotropic regarding their compressive modulus, ii) the applied welding force was constant (not sinusoidal), and iii) the hammering behavior of the sonotrode during the process was ignored (loss of contact between sonotrode and upper adherend).

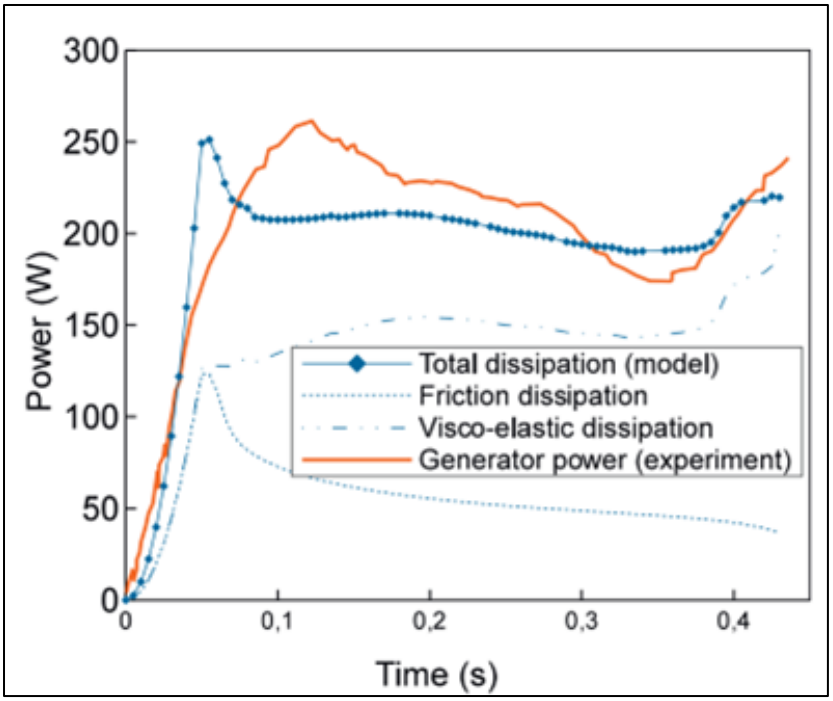


Figure 2.9. Reproduction of power dissipation in 1500 N/86.2 µm case for CF/PEI adherends investigated by Villegas et al. [31, 37].

Following this study, Palardy et al. developed on the existing model by investigating the hammering phenomenon due to periodic loss of contact in USW of TPCs. The authors proposed an experimental procedure to capture and study this behavior by performing static welding setup fitted with a high-frequency laser for the observation of the transmission of vibrations to the adherends. The 2D Comsol heat transfer model developed in [37] was updated and used to predict the power dissipation throughout the USW process. This update assumes that the welding overlap is the main source of power dissipation, and that the friction behavior of the two energy director interfaces are identical. The update employs three primary changes: i) the amplitude transmission from the sonotrode to the upper adherend was used instead of the hammering coefficient, ii) viscoelastic heating was considered, and iii) the simulation stopped when the minimum temperature in the energy director exceeded 315°C to

sufficiently capture the viscoelastic heating during the vibration phase. Experimentally, CF/PEI laminates were welded in a lap shear configuration with a neat rectangular PEI film (0.25 mm) as the energy director. The resulting measured amplitude was averaged at selected points over the process and applied to the newest version of the model. This change showed improved agreement between theoretical and experimental measurements for power consumption.

Yang et al. conducted a numerical study of temperature characterization in UW of CF/PA66 using thermomechanical finite-element modeling in both MATLAB and ANSYS [38]. For this model, frictional and viscoelastic heat generation as well as mass, stiffness, and damping matrices are updated in ANSYS and sent to MATLAB for dynamic analysis according to the updated mass/stiffness/damping properties. The displacement obtained through the dynamic analysis can then be used in determining the strain required for viscoelastic heat generation and stress required for frictional heat generation. The loss modulus can then be calculated according to the nodal temperatures determined by ANSYS thermal analysis. This process repeats until the end of the simulation. From this model, authors identified two primary states, contact and separation, at the welding interface in the early stages of welding. As the simulation progresses, the separation stage dissipates, and the user is left with a welded part.

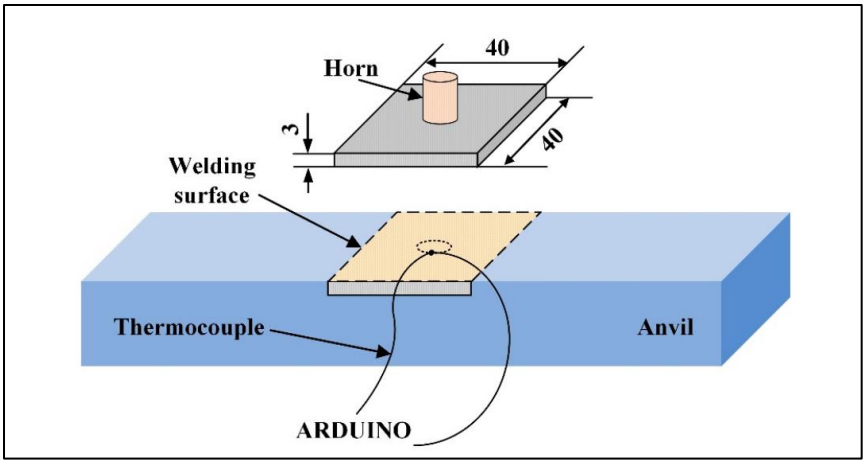


Figure 2.10. Schematic of experimental setup for temperature measurement of CF/PA6 composite specimens (shown in mm) [38].

Experimental validation involved a single K-type (0.125 mm) thermocouple placed at the interface between the horn and the welding surface (Figure 2.10). Using the following parameters, experimental welds were performed for comparison to the model: frequency 20 kHz, amplitude 35 µm, trigger force 200 N, plunging speed 0.3mm/s and welding time 0.5 s. Compared to a numerical dataset generated by the model, the experimental values showed good agreement with the simulation (Figure 2.11).

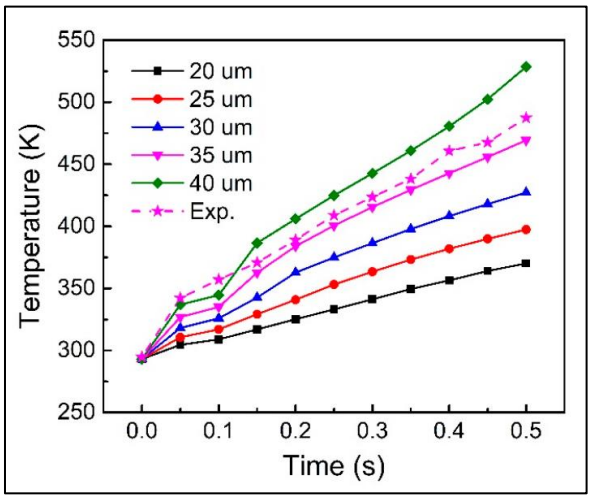


Figure 2.11. Node temperature on weld interface for various vibrational amplitudes [38].

### 2.2.2. Continuous Ultrasonic Consolidation

Continuous USC utilizes rotational and/or translational movement to facilitate in-situ impregnation and consolidation, much like traditional UAM. Rizzolo and Walczyk [28] proposed a simplified heat generation model based on surface energy pulse to predict temperature trends between plies for polyethylene terephthalate (PET)/CF specimens, but it showed differences by at least 30°C with experimental thermocouple data (Figure 2.12). The authors concluded that this model with a rule of mixtures approach to approximate material properties showed good agreement with the temperature just below the weld surface, but decreased in accuracy moving deeper into the laminate. Moreover, microstructural quality was not investigated at that stage.

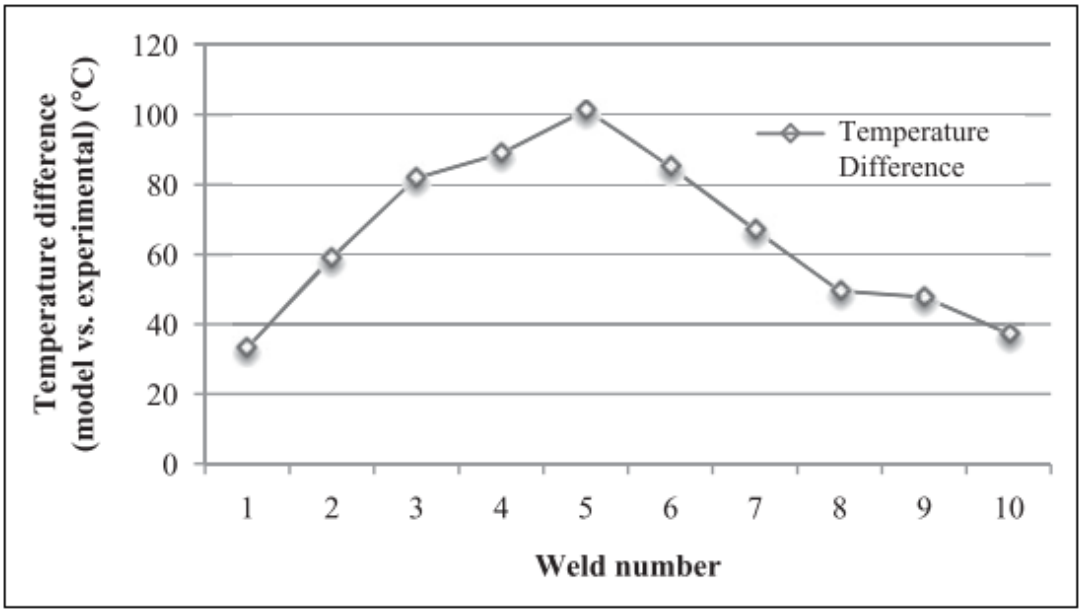


Figure 2.12. Temperature difference between model and corresponding weld trial measurement for quasi-isotropic layup PET/CF specimens [28].

Lionetto et al. [26, 27] developed a 2D finite element (FE) with Comsol Multiphysics to predict temperature distribution during USC of rovings, taking into consideration ultrasonic heat generation and power required to melt the PP matrix. The model neglected

the curvature of the mandrel, and the roving was represented as a single material with volumetrically averaged material properties taken from GF and PP components. A triangular moving mesh module was implemented to simulate the roving speed when rotating on the mandrel. Using a high-speed data acquisition system with a single needle-shaped type K (0.075 mm) thermocouple, temperature measurements were conducted on a 3-layer composite, with the thermocouple placed between layers 2 and 3 (Figure 2.13). Comparison between experimental and modeled results showed good agreement in terms of peak temperature (Figure 2.14).

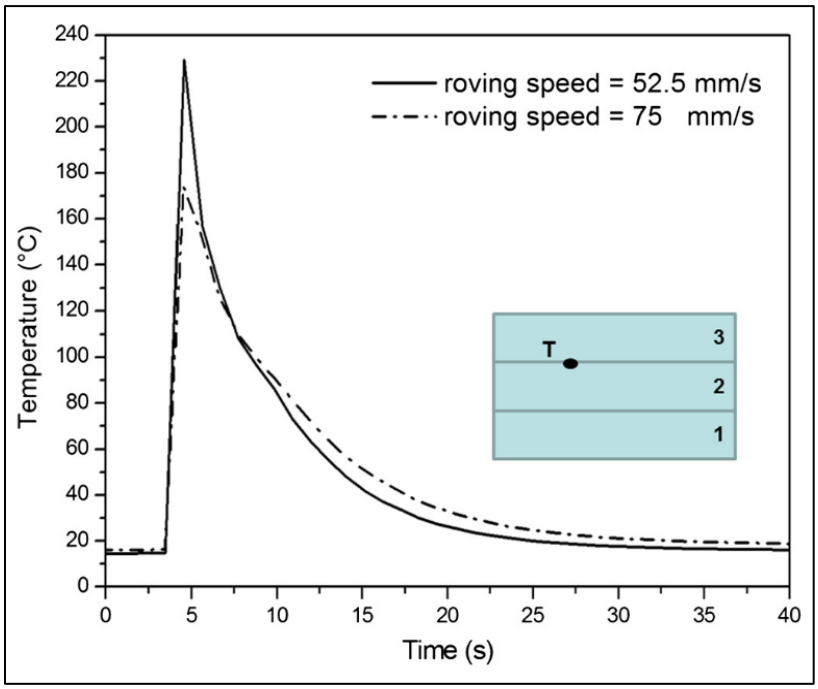


Figure 2.13. Plot of measured temperature evolution of GF/PP samples for two different roving speeds [27].

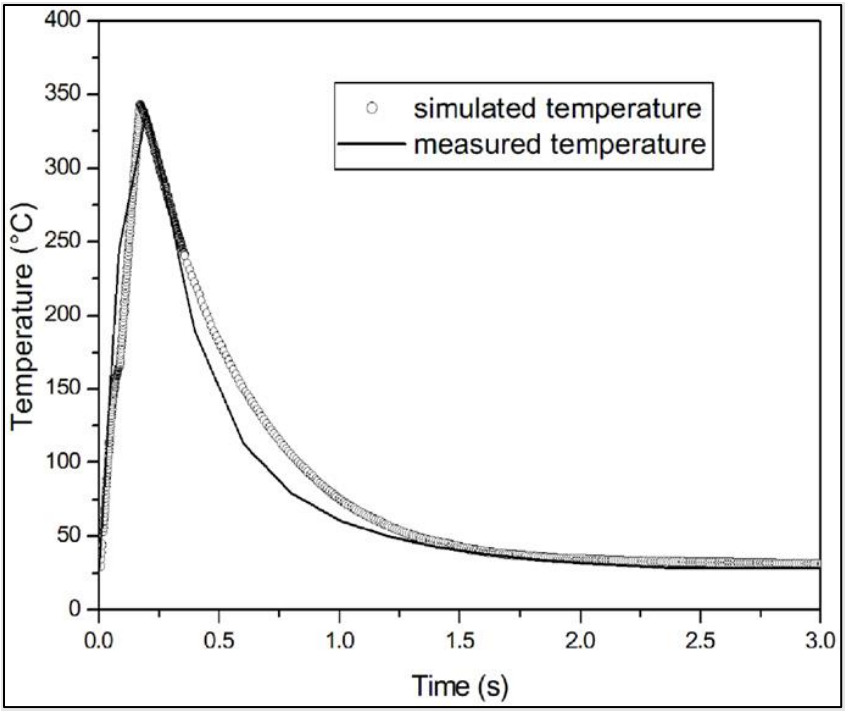

Figure 2.14. Plot of temperature distribution in the midplane of the GF/PP commingled roving during consolidation for different times [26].

Consolidated prototype cylinders were assessed by measuring their shear modulus ($G'_{12}$) by dynamic mechanical analysis (DMA) in torsion mode with a frequency sweep between 0.08 and 15 Hz and deformation amplitude of 0.016 % (90° to fiber direction). For comparison, compression molded samples were preheated to 200°C and molded at 10 bar for 30 seconds. Both consolidation methods yielded specimens of approximately equal density (1.419 ± 0.02 vs 1.420 ± 0.02 g/cm$^3$ for USC vs compression molding, respectively). The authors found a $G'_{12}$ of 935.22 ± 48 MPa for the cylinders and 989.36 ± 39 MPa for compression molded samples. Sample morphology was assessed with a scanning electron microscope (SEM), finding average void content of the cylinders to be 1.94 ± 0.5 %, slightly higher than compression molded samples (1.80 ± 0.5 %).

## 2.3. Research Gap

Overall, research gaps were identified in the literature regarding USC of TPCs. First, high temperature, high performance thermoplastic matrices have not been investigated (e.g., polyether ether ketone (PEEK), polyphenylene sulfide (PPS), or polyether imide (PEI)). It is assumed that the higher melting temperatures to consolidate such matrices would require significantly more power from the welder, possibly limiting its use. Second, most experimental studies are focused on UD fiber composites. Woven fabrics present additional challenges [39], for which micro-structural quality has not been explored experimentally with respect to USC. Finally, there is a lack of comprehensive thermal models for this process, including experimental validation at various locations across the samples. Prediction of temperature profile throughout specimens is valuable as it affects matrix melting, fiber impregnation and recrystallization behavior, and thus, quality of the final laminate.

# 3. EXPERIMENTAL METHODOLOGY

This chapter will describe the manufacturing methods and experimental procedures used throughout this study. In the order listed, the topics of discussion are materials, processing conditions, and characterization methods.

## 3.1. Materials

This study used Natural Fortron® polyphenylene sulfide (PPS) films (SKX-382, purchased from Professional Plastics, CA, USA) with a thickness of 0.08 mm and Toray T-300 standard modulus CF 3k twill weave fabric (purchased from Composite Envisions, WI, USA). The CF fabric has an areal density of 267 gsm. All sheets were pre-cut into 50 mm × 50 mm laminae prior to consolidation.

## 3.2. Manufacturing Methods

This section describes the machines and procedures used to fabricate the CF/PPS composite samples for both the USC and compression molding fabrication methods.

### 3.2.1. Ultrasonic Consolidation

A Rinco Ultrasonics Dynamic 3000 ultrasonic welder with a 40 mm-diameter cylindrical sonotrode was used to consolidate the CF and PPS layers at a frequency of 20 kHz, up to a maximum power of 3000 W. The vibrational amplitude was set to 38.1 $\mu$m and a consolidation force of 1000 N was used for all trials. Solidification force and holding time were set to 1000 N and 2000 ms respectively. The welding and solidification force correspond to a pressure of 0.8 MPa, which is in line with a typical pressure range applied during compression molding. The main process steps are shown in Figure 3.1, along with ply stacking sequence, which consists of three CF layers between four PPS

films in 0° orientation with a layer of polyimide film (Kapton®, American Durafilm, Holliston, USA) between the topmost PPS layer and the sonotrode face.

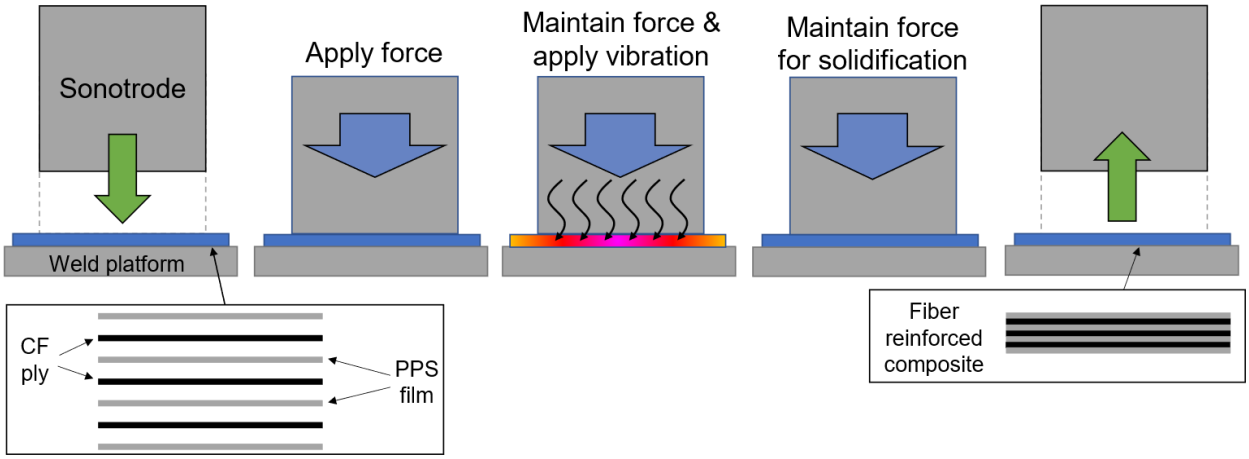


Figure 3.1. Schematic illustration of steps in USC process for creating fiber reinforced CF/PPS composite samples.

Welding parameters, and number of layers were selected based on preliminary results from a previous study, showing the effect of welding force and vertical sonotrode displacement on consolidation quality [2]. Sample size was sufficient to display representative behavior of the process under a single consolidation step [29]. The welding process was controlled in two ways: 1) downward vertical displacement of the sonotrode (also referred to as “travel”); and 2) vibration duration (weld time). Four travel values were considered: 0.11 mm, 0.15 mm, 0.20 mm, and 0.25 mm, based on preliminary trials producing consistent outputs.

To further assess the effect of control parameters on temperature profile and to confirm the predictive capabilities of the theoretical model, four vibration times were also selected to obtain experimental measurements during USC: 1000 ms, 1750 ms, 2500 ms, and 3250 ms. After consolidation, the welder provided four primary outputs, in addition to its power and displacement curves: weld time (ms), energy (J), maximum power (%), and

weld distance (mm). In both control modes, weld time is the primary input for the theoretical model.

### 3.2.2. Compression Molding

To create reference specimens, CF/PPS laminates were compression-molded using dry CF plies and PPS films in the same stacking sequence as shown in Figure 3.1. Samples were placed in a heated press (Dake, 75 ton) and consolidated at 320 °C at approximately 0.8 MPa pressure for 20 minutes, then cooled in the press under pressure.

## 3.3. Process Modeling for Ultrasonic Consolidation

This section discusses the MATLAB program used to generate a theoretical 2-dimenional (2D) temperature map throughout USC and cooling.

### 3.3.1. Governing Equations

#### *3.3.1.1. Heat Equation*

The general form of the heat equation used in this model is given by the 2D heat equation with heat generation $H$ via viscoelastic heating $Q$ (heat source) and melting energy of the PPS matrix $\dot{H}_m$ (heat sink), as shown in Eq. (1) [27]:

$$k\frac{\partial^2 T}{\partial x^2} + k\frac{\partial^2 T}{\partial y^2} + H = \rho C_p \frac{\partial T}{\partial t} \tag{1}$$

where $k$ is thermal conductivity, $\rho$ is density, $C_p$ is specific heat, and *H* is given by Eq. (2):

$$H = Q - \rho\dot{H}_m \tag{2}$$

#### *3.3.1.2. Viscoelastic Heating*

The heat generation term $Q$ represents the applied vibrational energy being dissipated as heat through intermolecular friction, also known as viscoelastic heating. $Q$

depends on the applied frequency $\omega$, the square of strain amplitude $\varepsilon_0$ of the ultrasonic vibration, and the loss modulus of the material $E''$, as shown in Eq. (3) [40]:

$$Q = \alpha \frac{\omega \varepsilon_0^2 E''}{2} \tag{3}$$

The factor $\alpha$ is a lumped, efficiency parameter that represents any losses from the translation of vibrational energy to heat (i.e. hammering, generator efficiency, acoustic losses, energy dissipation in specimen and clamping fixture) [37]. To capture thermal behavior, this factor was determined to be 0.15 based on literature [41], and comparison between theoretical and measured data points for several sets of weld parameters [42].

Using the time-temperature superposition method described by [37], the data was shifted to the 1 Hz master curve to obtain a shift factor that can be used to extrapolate to 20 kHz (see Section 3.4.1 for experimental procedure). With this technique, a temperature shift factor of $-24.02\,℃$ was obtained for 20 kHz, yielding $E'' = 0.028\,GPa$ at room temperature (see Appendix A for details). For this model, $E''$ is held constant at this value for all temperatures.

The strain amplitude $\varepsilon_0$ was determined based on a model from [43] stating that $\varepsilon_0$ is a function of the ratio of the moduli of the matrix and fiber layers. This method led to $\varepsilon_0 = .0127$ for this configuration (see Appendix B for calculation).

*3.3.1.3. Melting Heat*

The heat required to melt the PPS matrix $\dot{H}_m$ is a function of the degree of melting $X_m$ as shown in Eq. (4):

$$\dot{H}_m = H_T \frac{dX_m}{dt} \tag{4}$$

where $H_T$ is a reference value representing the total heat absorbed throughout the entire heating process, given by Eq. (5):

$$H_T = \int_{T_i}^{T_f} dH * dT \tag{5}$$

The degree of melting is defined by Eq. (6):

$$X_m(T) = \frac{H(T)}{H_T} \tag{6}$$

$X_m$ can be expressed by the statistical approach of [44] based on the assumption that the melting peak, obtained through differential scanning calorimetry (DSC), can be regarded as a statistical distribution of melting temperatures resulting from a distribution of lamellar thicknesses also known as the Richards function [45, 46]. This relation depends on the temperature at the peak of the DSC signal, $T_C$, an intensity factor $k_{mb}$, and a shape factor $d$. For simplicity, an alternative form of Richards equation from [47] was used, given by Eq. (7):

$$X_m(T) = \frac{X_{m,max}}{[1 + de^{-k_{mb}(T-T_C)}]^{\frac{1}{d}}} \tag{7}$$

where

$$\frac{dX_m}{dT} = X_{m,max} \frac{k_{mb} e^{(-k_{mb}(T-T_c))}}{[1 + de^{-k_{mb}(T-T_C)}]^{\frac{1}{d}+1}} \tag{8}$$

where $X_{m,max}$ is the maximum value calculated using DSC data points (see Section 3.4.2. for procedure). MATLAB's curve fitting tool was used to obtain a fit to the DSC data with $R^2 = 0.9963$ and $95\,\%$ confidence interval. The parameters were assigned the

corresponding values: $d = 0.6566$, $k_{mb} = 9.428$. The fit and its derivative were plotted against experimental data (Figure 3.2) for the range of measured temperatures.

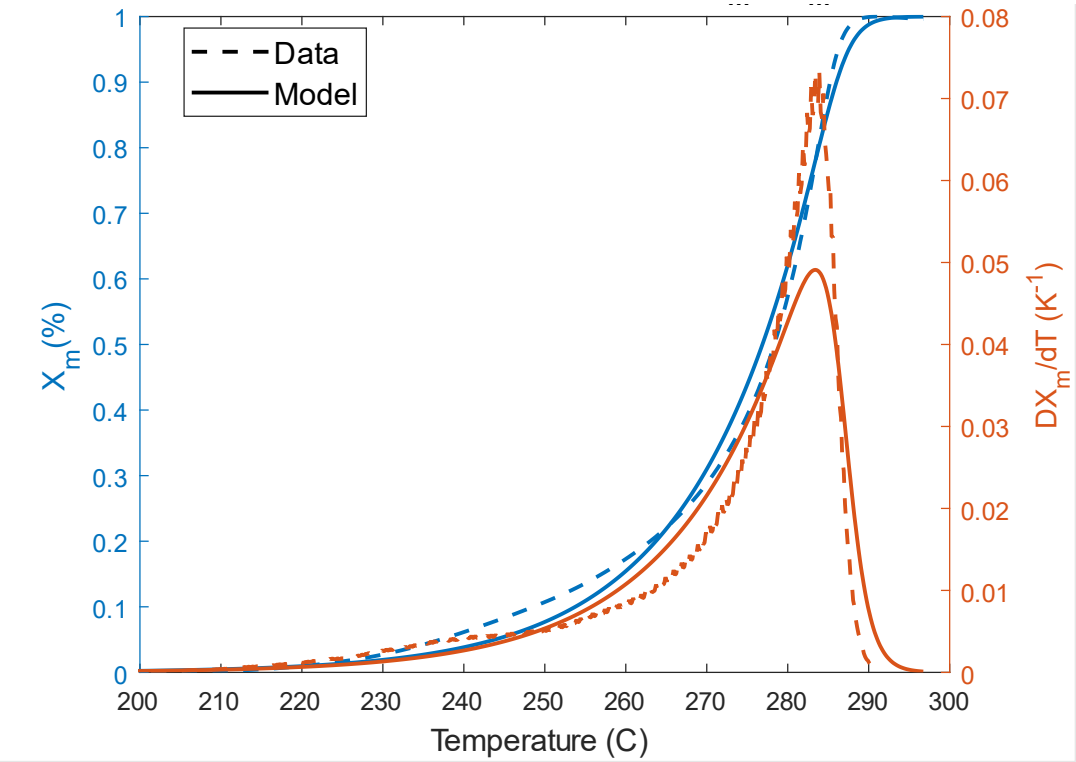


Figure 3.2. Measured data from DSC and curve-fit for PPS matrix degree of melting, $X_m$, and $dX_m/dT$.

The MATLAB PDE Solver was provided with a conditional statement that would set the heat sink term $\dot{H}_m = 0$ once the temperature reached $T_{melt} = 291.1\,℃ = 564.2\,K$, (corresponding to $X_m = 1$). The heat source term can be represented by the following piecewise function in Eq. (9):

$$H(T) = \begin{cases} Q - \rho(T)\dot{H}_m(T)\,, & T \le T_{melt} \\ Q, & T > T_{melt} \end{cases} \tag{9}$$

As shown in Eq. (10), a second conditional statement was set to assign the heat generation term $H = 0$ once $t_{weld}$ is achieved:

$$H = \begin{cases} H(T)\,, & 0 \le t \le t_{weld} \\ 0, & t > t_{weld} \end{cases} \tag{10}$$

*3.3.1.4. Material Properties*

To determine the composite material properties, a few assumptions were made for the simplified FE model implementation. The rule of mixtures was used with constituent properties shown in Table 3.1. To account for phase change, “dry” and “wet” states were introduced through the rule of mixtures in Eq. (11) to Eq. (14) for specific heat $C_p$ and thermal conductivity $k$ [26]:

$$k_{dry} = k_{pps}\Phi_{pps} + k_{CF}\Phi_{CF} + k_{air}\Phi_{air} \tag{11}$$

$$C_{p_{dry}} = C_{p_{pps}}\Phi_{pps} + C_{p_{CF}}\Phi_{CF} + C_{p_{air}}\Phi_{air} \tag{12}$$

$$k_{wet} = k_{pps}\Phi_{pps} + k_{CF}\Phi_{CF} \tag{13}$$

$$C_{p_{wet}} = C_{p_{pps}}\Phi_{pps} + C_{p_{CF}}\Phi_{CF} \tag{14}$$

where $\Phi_{pps}$, $\Phi_{CF}$, and $\Phi_{air}$ represent the volume fraction of PPS, carbon fiber, and air, respectively, and $\Phi_{air}$ is assumed to be 30 %.

The volume fractions were calculated using the overall volume of the dry constituents with $\Phi_{CF} = 0.5769$ and $\Phi_{pps} = 0.1758$. The composite specific heat $C_p$ and thermal conductivity $k$ along with matrix density $\rho_m$ were calculated using the rule of mixtures, which was assumed to represent material behavior for the simplified FE model, where $X_m$ represents the percentage of the material in the melted or “wet” phase, given by Eq. (15) to Eq. (17) [26]:

$$k = k_{dry}\big(1 - X_m(T)\big) + k_{wet}X_m(T) \tag{15}$$

$$C_p = C_{p_{dry}}\big(1 - X_m(T)\big) + C_{p_{wet}}X_m(T) \tag{16}$$

$$\rho_m = (\rho_m)_{dry}\big(1 - X_m(T)\big) + (\rho_m)_{wet}X_m(T) \tag{17}$$

During consolidation, a portion of the generated heat is conducted to the sonotrode and welding platform through direct contact. Since the PDE toolbox cannot discern surface contact, the heat generation term was specified as a volumetric heat source within the composite that directly contacts the sonotrode face and welding platform with material properties listed in Table 3.1. All faces contacting open air were prescribed a boundary condition (BC) of free convection at $T_\infty = 20\,℃ = 293.15\,K$ with $h = 5\,W/mK$. Adiabatic conditions were assumed at all other boundaries. This limitation also prohibits direct representation of the loss of contact between the sonotrode and the sample after the vibration phase is completed. To address this, the material properties of the sonotrode were changed to those of air following the holding time to represent the sonotrode lifting following USC.

Table 3.1. Sonotrode and welding platform material properties.

| | Sonotrode (titanium) | Welding platform (stainless steel) | Carbon fiber | PPS film | | Air |
|---|---|---|---|---|---|---|
| | | | | Liquid | Solid | |
| $\rho\ (kg/m^3)$ | 4507 | 7860 | 1760 | 1264 | 1082 | |
| $k(W/mK)$ | 18 | 15 | 10.46 | 0.30 | | 0.026 |
| $C_p(J/kgK)$ | 544 | 502 | 717 | 2000 | | 1005 |

### 3.3.2. Model Description

Utilizing the PDE Toolbox's Heat Transfer utility, the viscoelastic heating, melting heat and material properties were applied to the general form of the heat equation with temperature dependence. The program is written to solve for the temperature gradient over the mesh at each timestep until the simulation time reaches the user-specified value.

For its first iteration, the program uses the specified initial value for ambient temperature and takes the initial heat generation and time equal to zero. The initial material properties are also taken at ambient temperature. Over the first step, the value of $H$ is updated to reflect the initiation of the welding process based on the state of heat generation in the welding cycle. The PDE solver takes $H, \rho, C_p$ and $k$ as inputs and calculates the new nodal temperatures over the meshed area for the given timestep. These temperatures are used as the initial temperatures in the following timestep, giving updated values for $H(T), \rho(T), C_p(T)$ and $k(T)$, and the calculation is run again, storing the nodal temperatures each time. This process repeats until the sum of the timesteps reaches the user-defined limit $t_{lim}$.

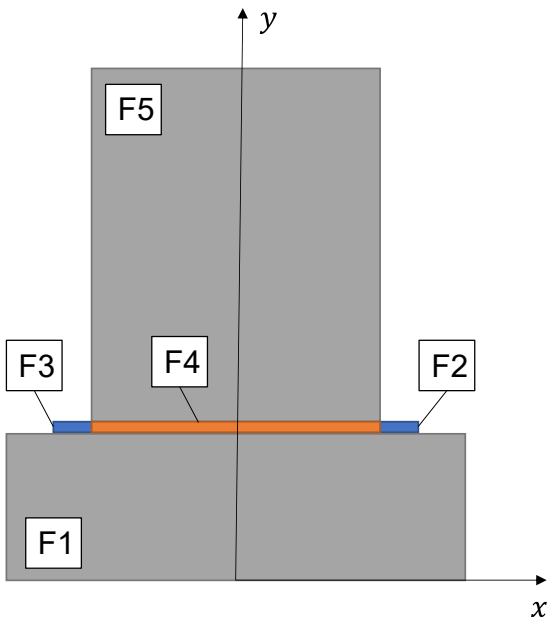


Figure 3.3. Geometry layout for heat generation model. See Table 3.2 for description of each component.

As shown in Figure 3.3, the cross-sectional geometry of the weld platform (F1), sample (F2, F3, F4) and sonotrode (F5) were specified as independent geometries with distinct material properties. The coordinate system is centered on the sample and all face

dimensions can be found in Table 3.2. The dimensions of F1 and height of F5 were chosen to sufficiently capture the conduction into each component from the heat source. The overall height of the sample (1.8 mm) was calculated using the combined pre-consolidated thicknesses of the CF and PPS layers. The sample was segmented into three parts, with F2 and F3 representing the outer perimeter that would remain unconsolidated, and F4 representing the projected area of the sonotrode in direct contact with the sample. The heat generation term $H$ is applied to F4 as a volumetric heat source. A quadratic mesh was generated over the entire shape shown in Figure 3.3 with element size $0.0021 < s < 0.0043$ and mesh gradation of 1.5.

Table 3.2. 2D FE model geometry dimensions.

| Representative component | | (F#) | Width (mm) | Height (mm) |
|---|---|---|---|---|
| Weld Platform | | 1 | 75 | 25 |
| Sample | Unconsolidated | 2,3 | 5 | 1.8 |
| | Consolidated | 4 | 40 | 1.8 |
| Sonotrode | | 5 | 40 | 50 |

For a given timestep size, the program will iteratively save nodal temperatures in a matrix over the simulation time, which are then plotted to a 2D heatmap for visualization. The user may input an overall simulation time greater than the weld time to observe the sample cooling after consolidation is complete. Temperature curves can be extracted at coordinates of interest for comparison to experimental temperature data. The MATLAB code used for this model can be found in Appendix E.

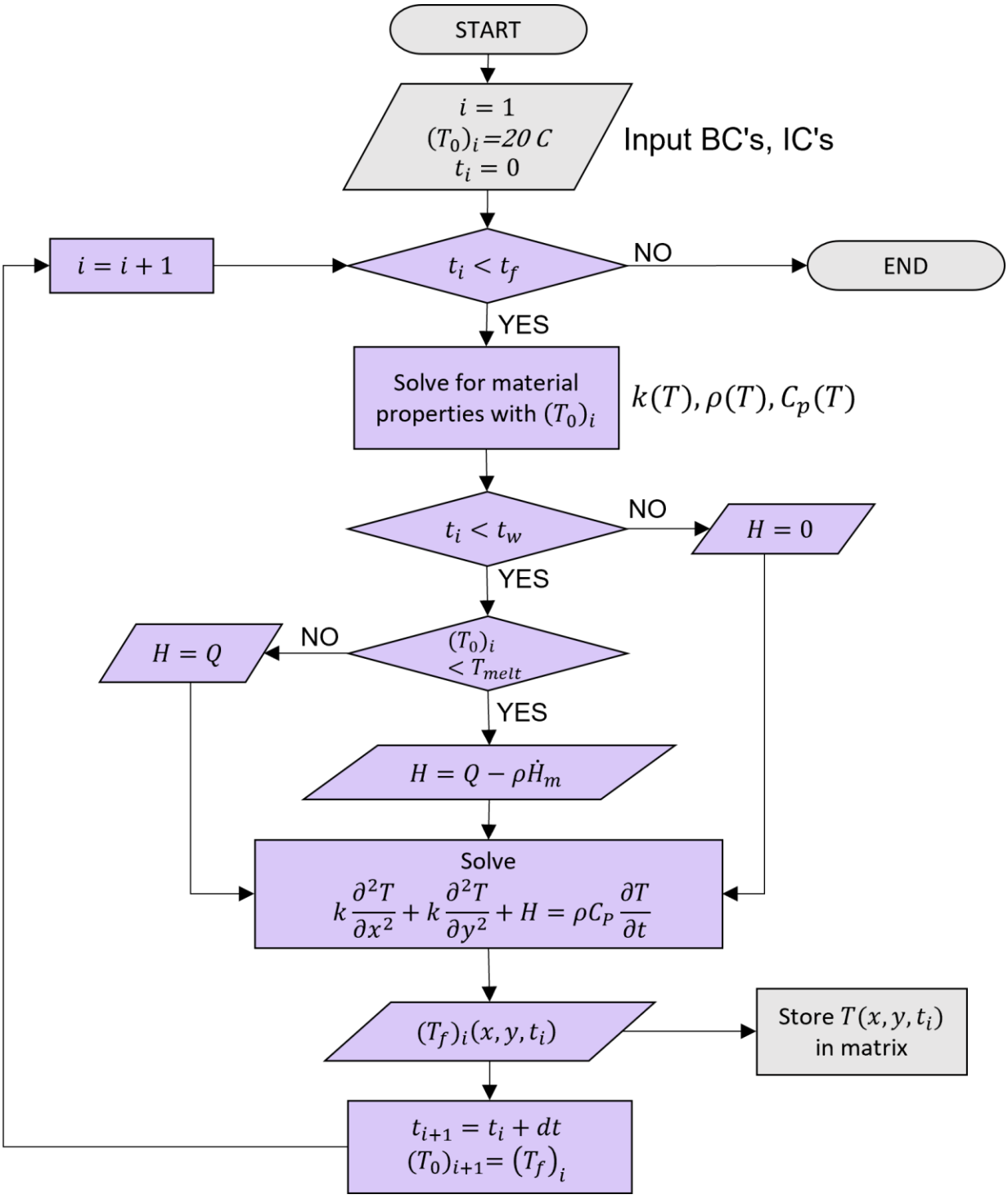


Figure 3.4. Flow logic diagram for code, starting from input boundary conditions (BC's) and initial conditions (IC's).

## 3.4. Characterization of Ultrasonically Consolidated Thermoplastic Composites

This section describes the methods used to assess the accuracy of the model and subsequent quality of consolidated specimens.

### 3.4.1. Dynamic Mechanical Analysis (DMA)

The loss modulus $E''$ for the PPS film was measured using a dynamic mechanical analyzer (TA Instruments Q800 DMA) apparatus from ambient temperature to 160 °C at frequencies of 0.1, 1, 10, and 100 Hz. Film specimens were cut into 18 mm x 8 mm rectangular samples and clamped with a torque of 0.34 Nm between the tensile fixture of the DMA.

### 3.4.2. Dynamic Scanning Calorimetry (DSC)

A 3.35 mg PPS film sample was sealed in the test chamber, initialized at 30 °C, and purged with nitrogen at 20 mL/min. The sample was heated from 30 °C to 300 °C at 10 °C/min and held at 300 °C for 1 minute, then cooled from 300 °C to 30 °C at 10 °C/min and held at 30 °C for 1 minute. This cycle was completed 2 times in total.

### 3.4.3. Thermal Characterization

To validate the theoretical temperature profiles, direct thermocouple measurements between plies were acquired, as illustrated in Figure 3.5. K-type thermocouples (36 AWG gauge wire purchased from Omega Engineering, Norwalk, CT, USA) were stripped and placed in three locations throughout the sample (N1, N2, N3) and taped flush to the platform, ensuring minimal interference with the perceived thickness of the sample. It is to be noted that the insertion of more than three thermocouples created issues with the welding process as their total thickness affected the compaction and flow of the stacked plies. Thermocouples were connected to a PC

through a Model DI-2008 Thermocouple and Voltage DAQ and Data Logger System to store temperature data. Measurements were taken at a sampling rate of 67 samples per second.

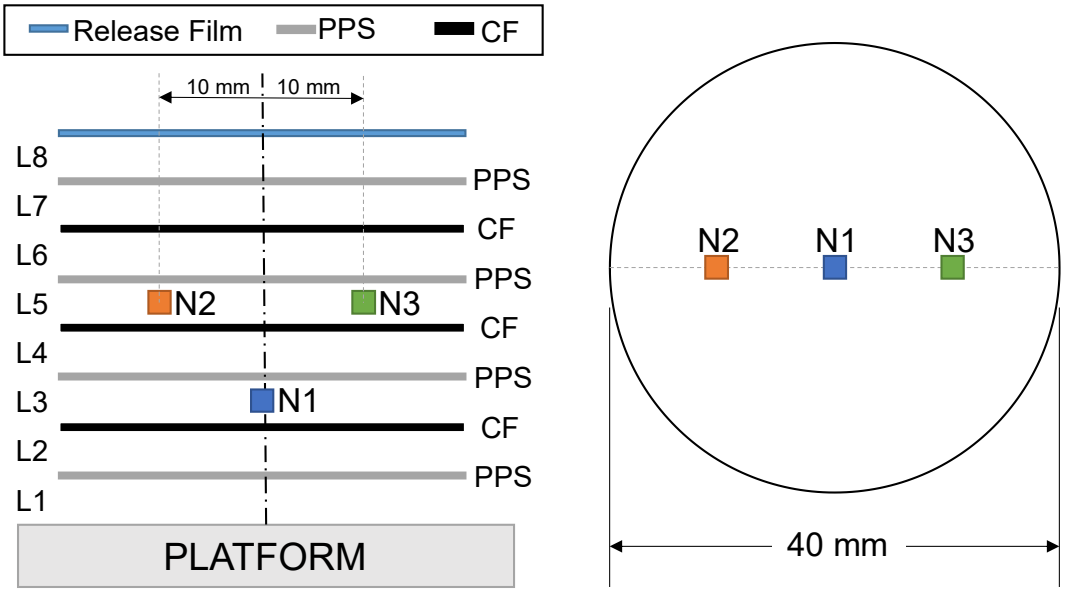


Figure 3.5. Ply stacking sequence with in-situ thermocouple layout (left) and top view of thermocouple layout (right).

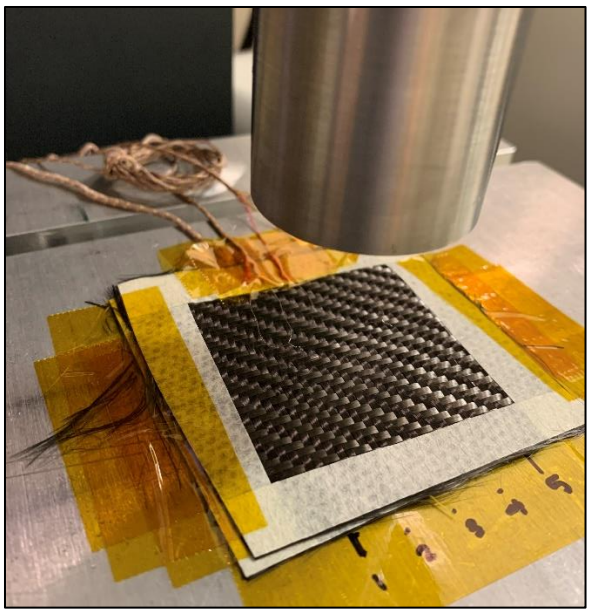

Figure 3.6. Thermocouples positioned within plies prior to consolidation.

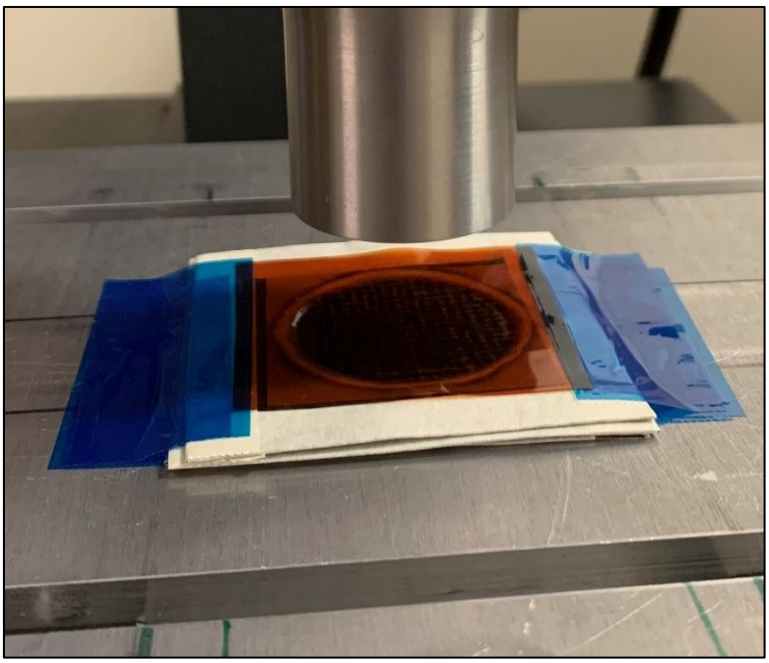

Figure 3.7. CF/PPS specimen post-consolidation on weld platform.

Thermal imaging using a Teledyne FLIR A325sc infrared camera (FLIR Systems, Spicewood, TX, USA) was conducted in early stages of testing as a secondary validation step, but only provided temperature information at the outer perimeter of the sonotrode during consolidation and over the consolidated area once the USC process was completed. Captured videos were processed with FLIR Thermal Studio software for temperature identification and cross-examination with thermocouple measurements. Representative results are shown and discussed in Appendix C.

### 3.4.4. Microstructural Characterization

Void content of the samples was characterized with a desktop cone-beam micro-Computed Tomography (μCT) scanner (Scanco Model 40, Switzerland). Specimens for the four trials were cut into 10 mm × 10 mm segments from the center of each consolidated sample. 3D reconstruction was performed with Avizo software from Thermo Fisher Scientific. Over ten DICOM slices were taken from each scan and analyzed with

ImageJ software (version 1.8.0, National Institutes of Health) brightness thresholding to determine average void content for each sample. It is to be noted that frayed edges were observed in some cases, which were not considered in the overall void content assessment.

Due to limited access to μCT scanning, optical microscopy was used for measuring void content of compression molded specimens and as a secondary validation method for void content percentages obtained from μCT. Samples were cut and mounted in an epoxy mold. They were grinded with 180, 360, 600, 800, and 1200 grit SiC abrasive pads, then polished with 6 and 1 μm diamond solutions. Images were captured at 10X magnitude with a Meiji MT8100 fitted with a Teledyne INFINITY microscope camera. Each photo was analyzed with ImageJ software to determine void content. Representative images used for void content calculations can be found in Appendix D.

# 4. RESULTS AND DISCUSSION

## 4.1. Thermal Characterization

The FE model provides the temperature profile throughout the specimen during matrix melting, consolidation, and cooling. Having the ability to predict the temperature distribution in the composite is highly valuable, as it strongly affects impregnation and recrystallization, and therefore, quality of the final laminate. Several cases were considered for simulations and a representative example of the 2D temperature distribution at different time values (*t*) is shown in Figure 4.1 for a full weld cycle (sample consolidated under 1000 N and a travel of 0.20 mm). During the welding process (from Figure 4.1B to C), the centerline (axial) temperature of the specimen exceeds the melting temperature of the PPS matrix (above 280 $^{o}$C) in the mid-plane of the sample. The temperature continues to increase until the sonotrode vibration is switched off (Figure 4.1C) and maintains a normal force of 1000 N for an additional 2 seconds. The sonotrode is then lifted (Figure 4.1D), allowing the specimen to further cool down until the simulation concludes (10 s).

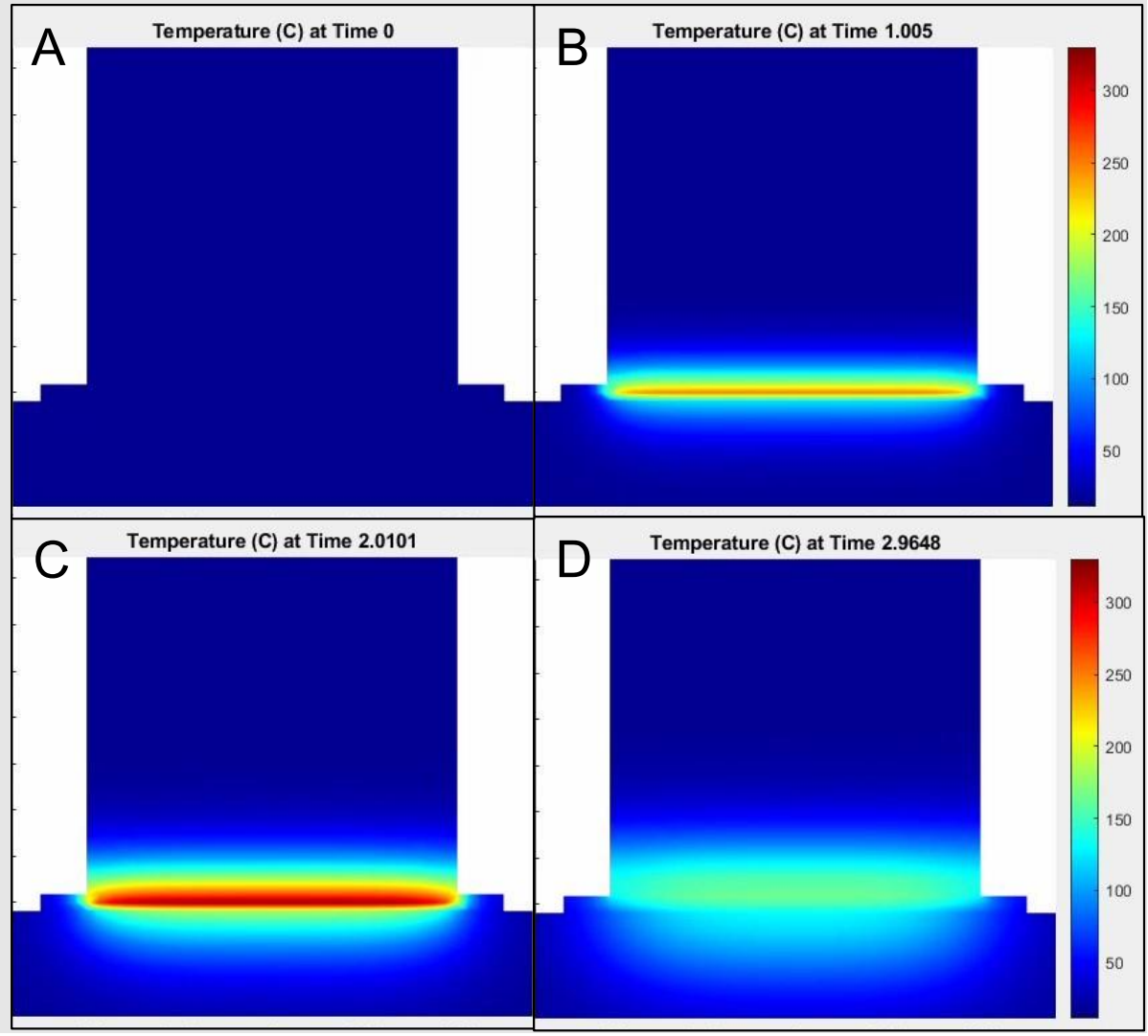


Figure 4.1. Temperature gradient progression at different time values (in seconds) for welding conditions of 1000 N and 0.20 mm travel: A) before weld, B) during weld, C) at peak temperature (end of weld), and D) post-weld cooling (solidification phase).

To assess agreement between predictive model and experiments, USC was conducted in two sets, as listed in Table 4.1: the first with sonotrode travel as the control parameter (Trials 1-4) and the second with weld time as the control parameter (Trials 5-8). The temperature profiles were measured with K-type thermocouples approximately placed at three nodes of interest (as shown in Figure 3.5) to assess the effect of position and the experimental variability. Welder output values (weld time, weld distance, energy,

and maximum power) are summarized in Table 4.1 for each trial. It is to be noted that the weld time in Trial 1 (0.11 mm travel) is higher than that of Trials 2 and 3. This discrepancy is likely due to inconsistencies in the perceived downward displacement of the machine. For very low travel values (< 0.10 mm), it was observed that the welder would often execute the maximum allowable weld time (10 s), leading to an incomplete welding procedure. To maintain a data point for a low desired travel, the first trial was designated a travel value of 0.11 mm, but still exhibited higher weld time than expected. It is assumed that the presence of thermocouples throughout the samples may have affected the perceived travel, as the wires thickness is on the same order of magnitude as the overall travel (~0.12 mm).

Simulation results were compared with experiments for all trials listed in Table 4.1. It is worth mentioning that the FE simulations for the travel-control trials (1-4) were carried out after the experiments took place, as the weld time is governed by the final vertical displacement of the sonotrode (i.e. weld distance in Table 4.1). For the corresponding simulations, time was employed as the input parameter. Temperature profiles at coordinates corresponding to each thermocouple node were extracted from the FE model and plotted with experimental data for Trials 1-4 (Figure 4.2-4.4). Horizontal lines corresponding to "total melting" of the PPS matrix ($X_m = 1$ at $T_{melt}$) are denoted on each plot. For all cases, nodal temperatures met and exceeded the melting temperature of the PPS matrix except for Node 1 in the 0.11mm case, which read a peak temperature of approximately 278 $^{o}$C at 2386 ms. In fact, peak temperatures at Node 1 for all cases are the lowest of the three nodes. Since the thermocouple placed at Node 1 is closer to the platform than Nodes 2 and 3 (Figure 3.5), it is possibly less affected by the heat generated

at the sonotrode interface and therefore experiences a smaller rise in temperature. This behavior was also reported for USC of thermoset prepregs similar to automatic fiber placement [48], including repair applications [49]. The FE model has potential to capture this behavior as the heat generation is volumetric within the sample geometry.

Table 4.1. Travel, weld time, weld distance, energy consumption and maximum power for all experimental trials.

| Trial # | Travel (mm) | Weld time (ms) | Weld distance** (mm) | Energy (J) | Max. power (%) |
|---|---|---|---|---|---|
| 1 | 0.11* | 2386 | 0.19 | 2794 | 44 |
| 2 | 0.15* | 1903 | 0.24 | 2250 | 43 |
| 3 | 0.20* | 2147 | 0.28 | 2593 | 44 |
| 4 | 0.25* | 3814 | 0.28 | 4370 | 43 |
| 5 | - | 1000* | 0.26 | 1123 | 44 |
| 6 | - | 1750* | 0.25 | 2056 | 44 |
| 7 | - | 2500* | 0.27 | 2939 | 43 |
| 8 | - | 3250* | 0.30 | 3790 | 43 |

* Indicates input value used on the welder.

** The final travel value provided by the welder at the end of the 2 s holding phase.

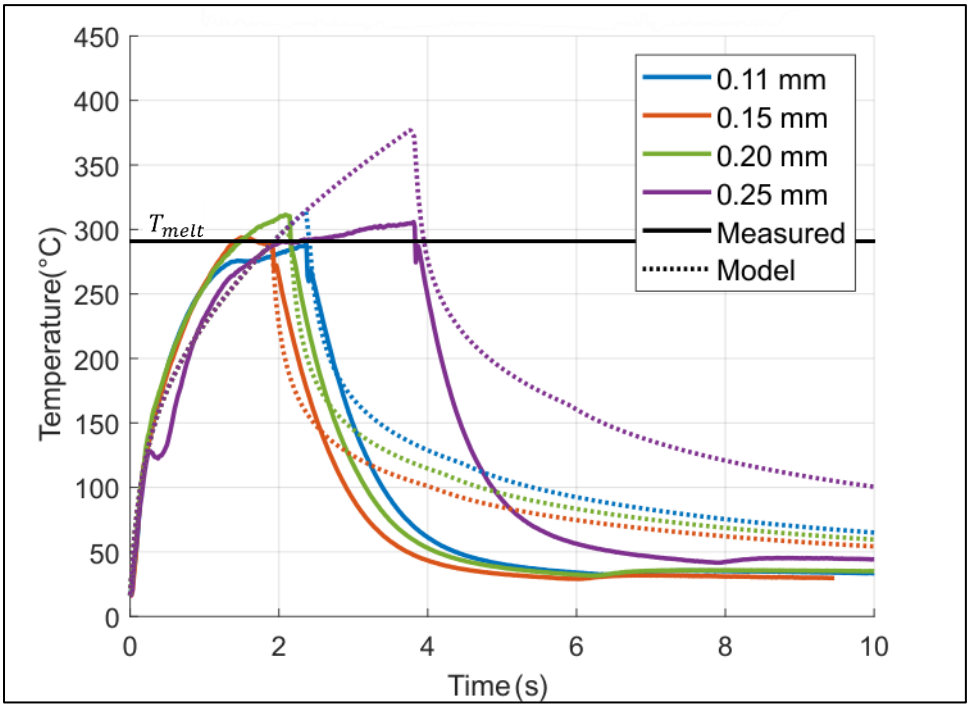


Figure 4.2. Representative temperature profiles for travel-control trials (Trials 1-4 in Table 4.1) at Node 1.

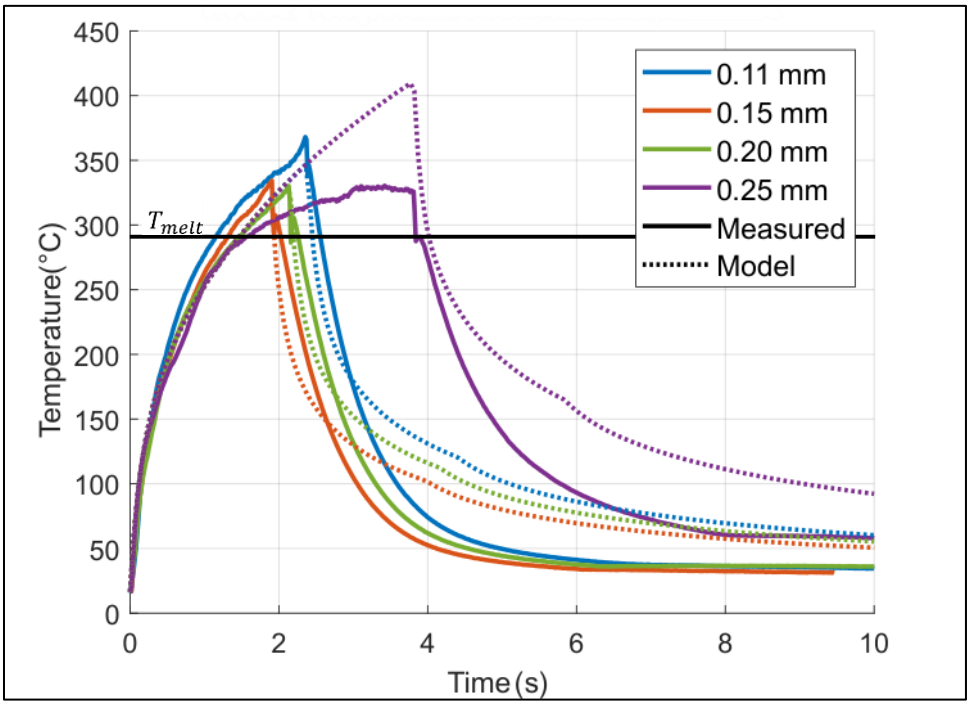


Figure 4.3. Representative temperature profiles for travel-control trials (Trials 1-4 in Table 4.1) at Node 2.

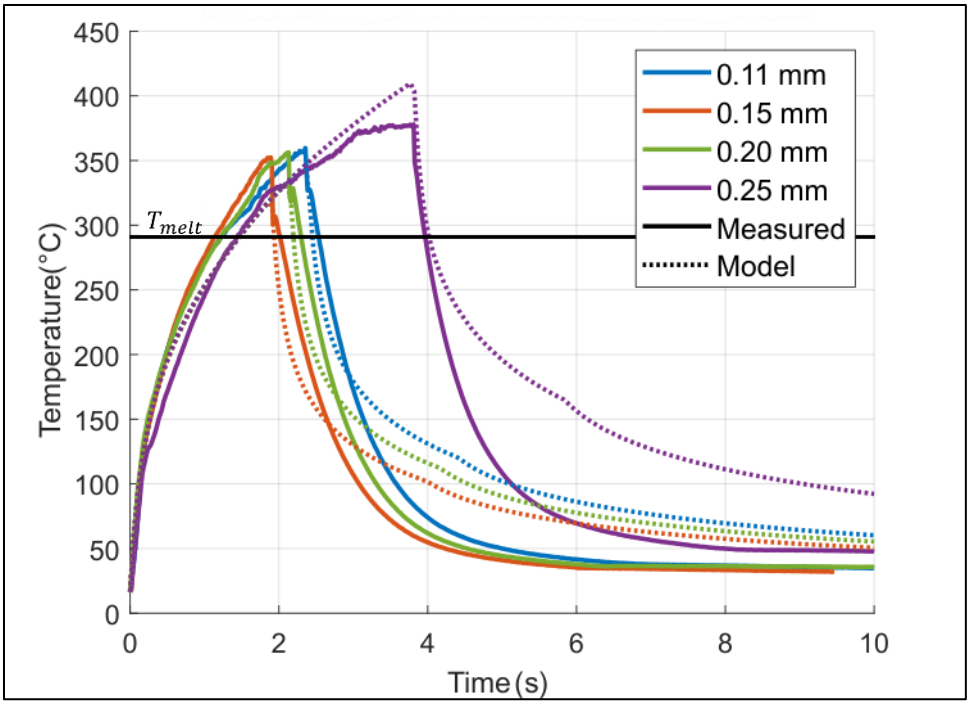


Figure 4.4. Representative temperature profiles for travel-control trials (Trials 1-4 in Table 4.1) at Node 3.

In general, higher travel values (and therefore longer weld times) resulted in higher measured peak temperatures at each node for the travel-control trials. Good agreement between experiments and modeled temperature profiles in the heating phase until peak temperature is observed (Figure 4.2-4.4), except for Node 1 and Node 2 for the 0.25 mm case. Differences such as these are likely caused by unavoidable thermocouple movement and/or polymer flow over the thermocouple tip during compaction, resulting from the highest travel value (corresponding to the most significant polymer flow). Furthermore, it can be observed that Node 2 and Node 3 do not exhibit symmetry in their experimental temperature profiles, suggesting minor misalignment between the sonotrode and the platform.

Similar observations can be made for the results of the time-control trials (Trials 5-8 in Table 4.1), as seen in Figure 4.5-4.7. Good agreement between experiments and

simulations is observed for Node 2 and Node 3 in the heating phase until peak temperature, while thermocouple measurements at Node 1 for the two longest weld times displayed similar differences as observed in Figure 4.2, Figure 4.3. As previously observed for travel-controlled trials, this is likely experimental error, caused by unavoidable thermocouple misalignment and/or movement during polymer flow and compaction.

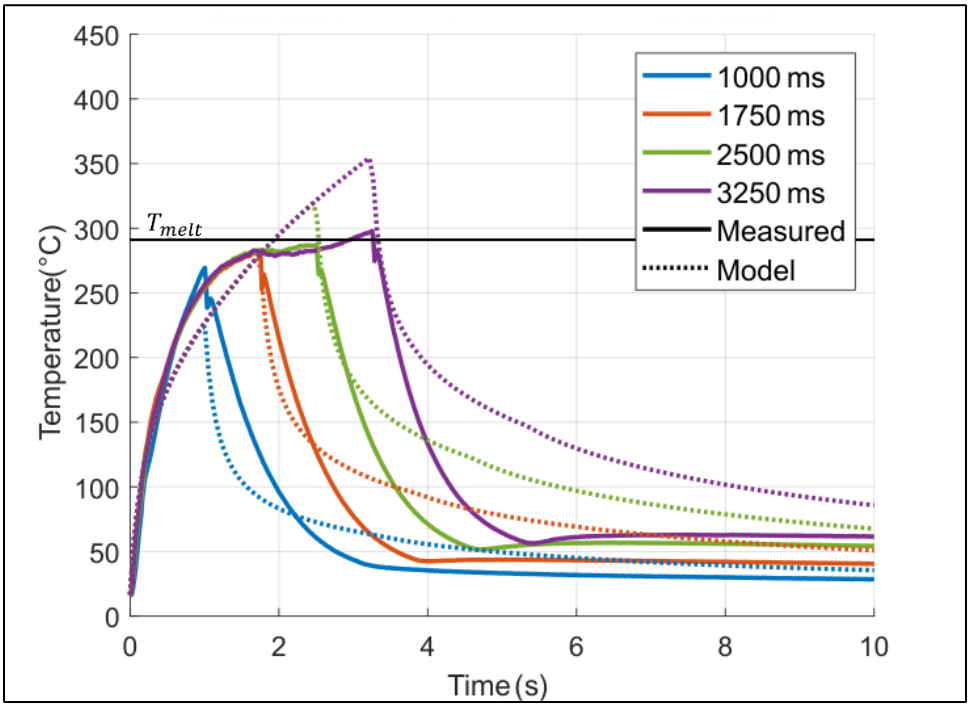


Figure 4.5. Representative temperature profiles for time-control trials (Trials 5-8 in Table 4.1) at Node 1.

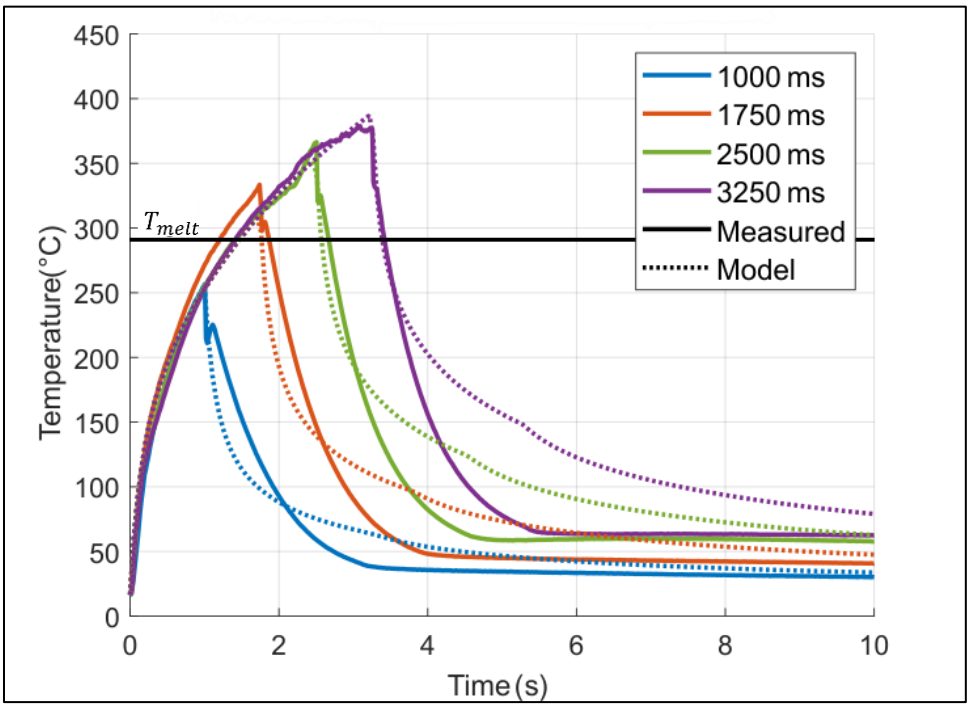


Figure 4.6. Representative temperature profiles for time-control trials (Trials 5-8 in Table 4.1) at Node 2.

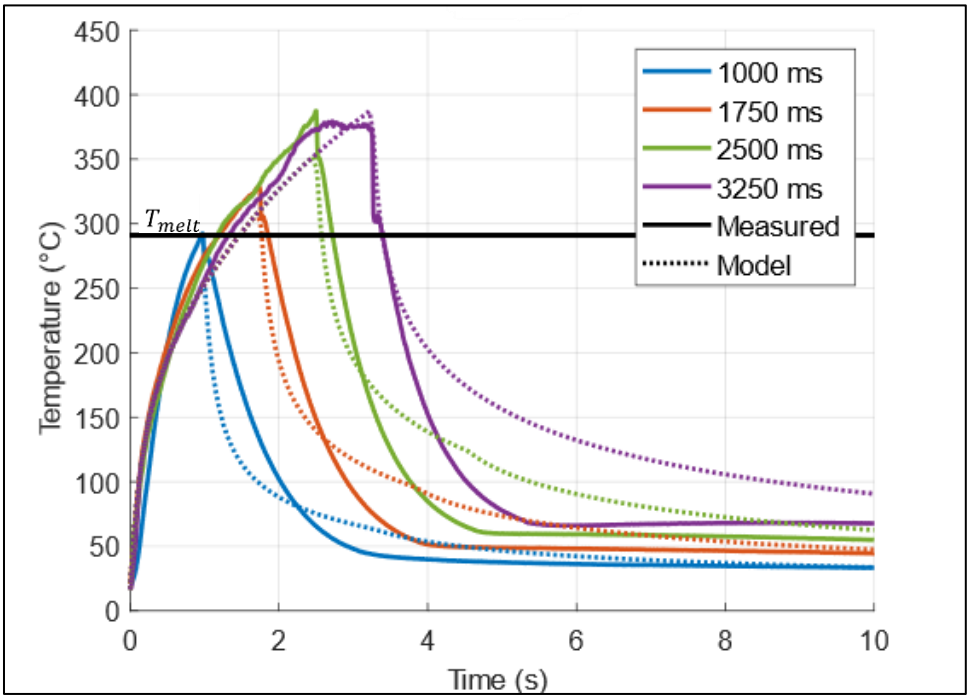


Figure 4.7. Representative temperature profiles for time-control trials (Trials 5-8 in Table 4.1) at Node 3.

In general, the model adequately predicted the heating behavior for each case, and peak temperature (or heating cutoff) was determined by the weld time. On the other hand, the predicted cooling behavior for all cases generally showed good agreement for temperatures above the melting point but deviated from the experimental profiles over time. The cooling rate for all samples in the FE model was lower than the experimentally measured cooling (ranging from approximately 70 $^{o}$C/s to 108 $^{o}$C/s as calculated in the initial linear region of the cooling phase). A likely contributing factor for this discrepancy is that the model does not account for the flow of matrix material throughout consolidation. The sample may experience enhanced cooling due to the convective effects of viscous flow within the molten matrix during the solidification phase.

### 4.2. Residence Time

As previously observed in Figure 4.2-4.7, the simulated temperature profiles generated for each set of weld parameters generally showed good agreement with experimental data in the vibration phase. This study is concerned with relating temperature profiles (modeled and experimentally measured) to quality of the consolidated specimens. It can be inferred that the amount of time the melted matrix is allowed to flow within the sample is directly related to the extent of impregnation of the dry CF plies, and therefore has a direct impact on the void content of the consolidated specimen. Thus, a parameter called residence time ($t_r$) was defined as the amount of time the PPS matrix spent above the melting temperature ($T_{melt}$) at a given location in the material. Figure 4.8 illustrates the residence time, $t_r$, for Node 2 at the longest weld time for time-controlled trials.

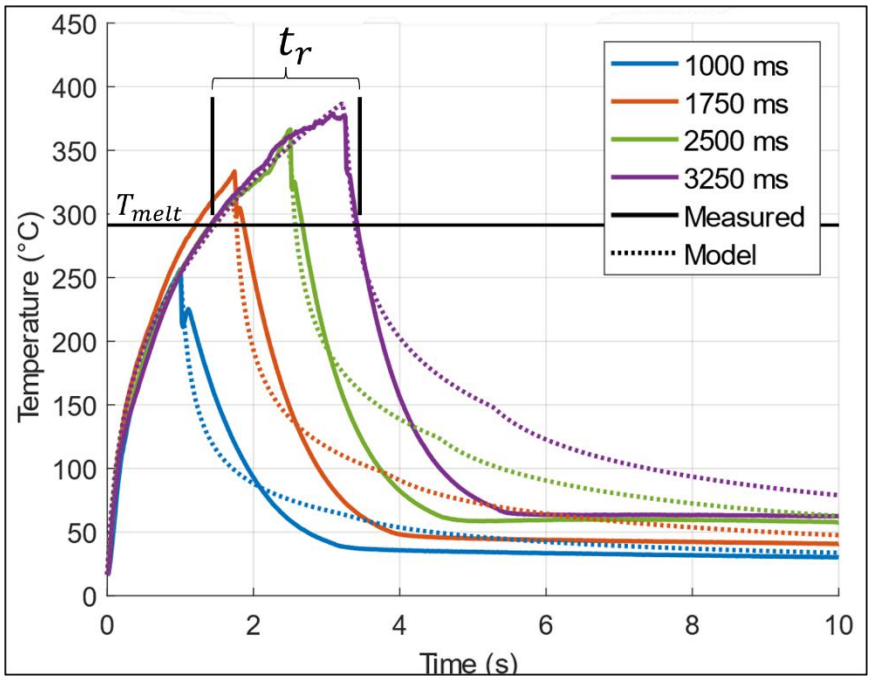


Figure 4.8. Graphical depiction of residence time ($t_r$) for longest weld time at Node 2 for time-control trials.

Comparison between the simulated and experimental residence time ($t_r$) above the melting temperature ($T_{melt}$) at Node 2 for travel control (Figure 4.3) and time control (Figure 4.6) trials is shown in Figure 4.9.

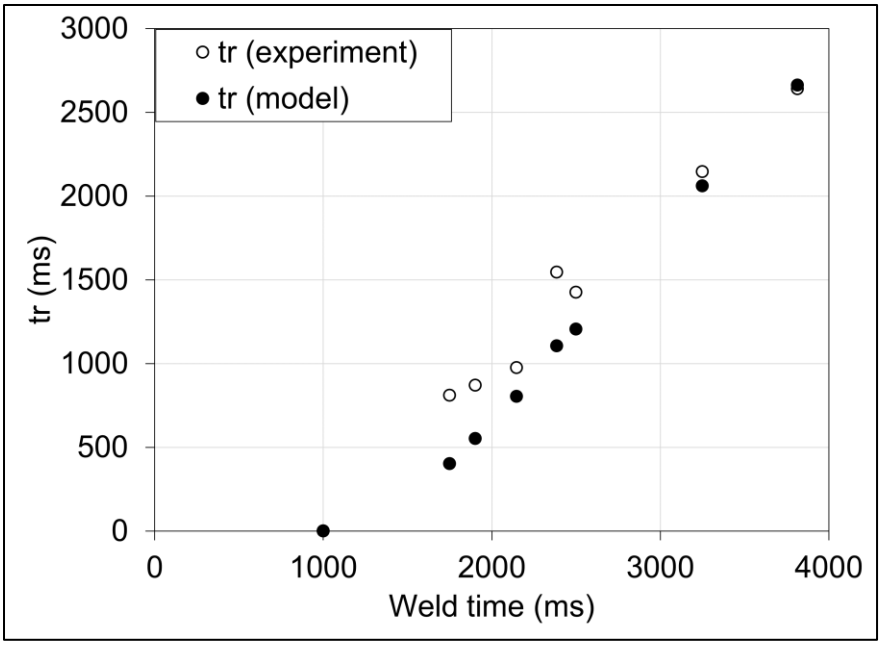


Figure 4.9. Comparison between experimental and simulated residence time ($t_r$) above melting temperature with respect to total weld time for travel and time-input trials (representative data is shown for Node 2).

In most cases, an error lower than 10 % was estimated for travel and time control modes. Similar results were obtained for other node locations. This implies that the model can adequately predict the evolution of the matrix phase change and the amount of time the matrix remains in the melted state near the center of the sample (through-the-thickness), confirming the validity of the developed FE model.

### 4.3. Microstructural Characterization

Figure 4.10 shows representative μCT cross-sections for travel-based samples (Trials 1-4 in Table 4.1) 0.15 mm travel (Figure 4.10A) and 0.25 mm travel (Figure 4.10B). Figure 4.11 illustrates a full 3D reconstruction from μCT imaging for one of the worst-case trials (0.15 mm travel). Voids within the resin-rich areas (lighter-colored PPS matrix) were generally concentrated toward the top of the samples (closer to the sonotrode interface), likely due to air bubbles moving to the surface of the molten PPS during polymer flow. In

some cases, the bottom film did not fully melt, indicating it was not sufficiently heated to facilitate flow, as seen at the bottom of Figure 4.10.

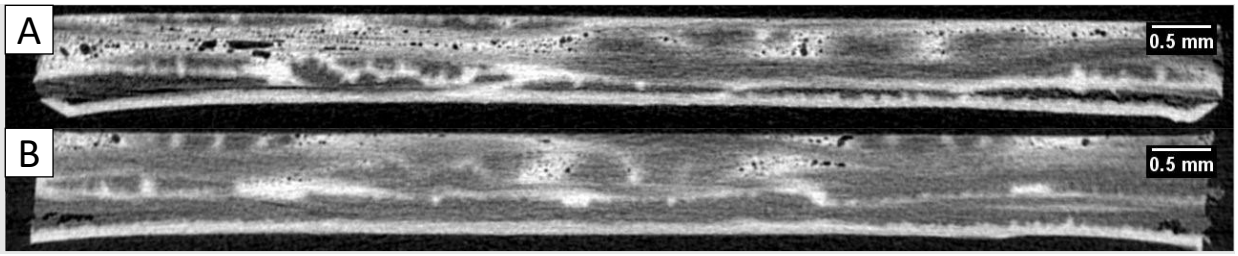


Figure 4.10. Representative μCT slices for A) 0.15 mm travel and B) 0.25 mm travel CF/PPS samples.

Table 4.2 summarizes the average void content for all travel-based trials. The 0.25 mm samples exhibited the lowest estimated void content (2.43 %), with the lowest standard deviation (0.81 %). Conversely, the 0.15 mm samples had the highest estimated void content (6.41 %). The welder outputs in Table 3 indicate that the weld time for the 0.15 mm trials was the lowest. It is also clear from the nodal temperature plots in Figures Figure 4.2Figure 4.4 that the 0.15 mm specimen remained above the melting temperature for the smallest amount of time compared to other trials. This information suggests that the high void content in the 0.15 mm samples was likely due to insufficient time allowed for polymer flow, preventing air from migrating and escaping before re-solidification took place. By the same logic, the PPS matrix of the 0.25 mm sample spent the longest amount of time in the melted phase, allowing sufficient flow and more air bubbles to move out of the plies before the cooling phase began. Overall, it is possible to reach void contents < 4% through USC for woven specimens, similarly to what was measured for unidirectional rovings [36]. However, μCT might not have fully captured the extent of micro-voids within the fiber bundles, which could further increase the actual porosity content. These results are consistent with averages found in previous CF/PPS samples [26]. Compression

molded specimens, as described in Section 3.2.2, were used as a comparison with the USC method. Void content was estimated as 1.68 ± 0.61 % through cross-sectional optical microscopy (See Appendix D for representative images).

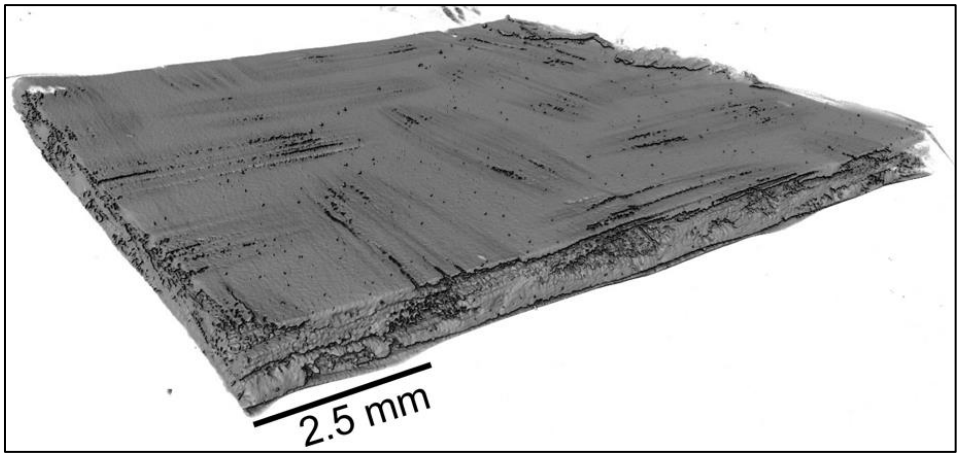


Figure 4.11. 3D reconstruction of a low-quality 0.15 mm CF/PPS sample from μCT imaging.

Table 4.2. Average void content for all travel-input and reference samples.

| | μCT Imaging | | Optical Microscopy | |
|---|---|---|---|---|
| Sample travel / Weld time | Average void content (%) | Standard deviation (%) | Average void content (%) | Standard deviation (%) |
| 0.11 mm / 2386 ms | 3.82 | 1.84 | 3.88 | 1.92 |
| 0.15 mm / 1903 ms | 6.41 | 1.90 | 4.54 | 1.45 |
| 0.20 mm / 2147 ms | 4.02 | 1.32 | 3.27 | 0.25 |
| 0.25 mm / 3814 ms | 2.43 | 0.81 | 2.57 | 1.25 |
| Compression molded (reference) | - | - | 1.68 | 0.61 |

For all samples that underwent void content analysis, longer weld times (and subsequent extended periods of liquid-phase polymer flow of the matrix) yielded specimens with lower void content, as illustrated in Figure 4.12. When comparing weld time data from Table 4.1 with void content from Table 4.2, it is observed the latter generally decreased (6.41 – 2.43 % in μCT, 4.54 – 2.53 % in optical microscopy) with an

increase in weld time (from approximately 1903 ms to 3814 ms). This corresponds to residence times above $T_{melt}$ of 870 ms to 2640 ms. A residence time above 2600 ms was sufficient to eliminate macro-voids (between CF layers) and consolidate the layers, but some micro-voids remained within the fiber tows. Nevertheless, the model presented in this thesis can be used to reasonably estimate process parameters as it allows prediction of the residence time for a given polymer matrix, according to weld time used to control the consolidation process.

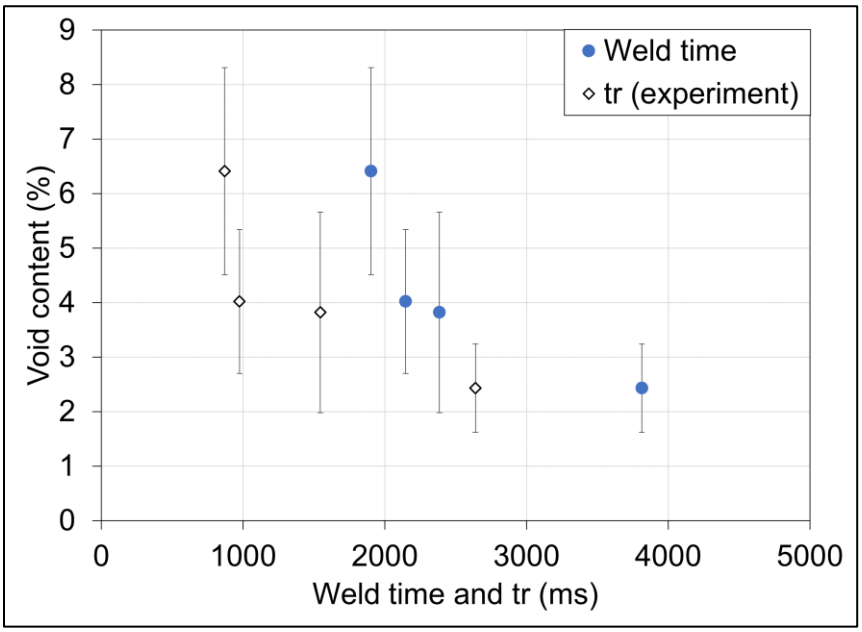


Figure 4.12. Void content with respect to weld time and experimental residence time ($t_r$) for travel-input trials (representative data is shown for Node 2).

# 5. CONCLUSIONS AND FUTURE WORK

## 5.1. Conclusions

In this study, USC of dry CF plies with high-temperature PPS films was investigated with respect to two main objectives: 1) develop a simplified FE model to predict cross-sectional temperature profile providing guidelines for experimental parameters selection (i.e., weld time); and 2) further understand the effect of ultrasonic parameters on micro-structural quality based on thermal history. To this end, a 2D finite element model was implemented to compute the temperature distribution in layered CF/PPS TPCs during USC. The model took into consideration melting behavior of the PPS matrix, viscoelastic heat generation, and control of the process through time or travel (vertical displacement of the sonotrode). Melting behavior was used to determine the degree of melting of the PPS matrix (i.e. average phase) at each timestep throughout the consolidation process to assign appropriate material properties. Viscoelastic heat generation, found as a function of vibrational frequency $\omega$, material strain amplitude $\varepsilon_0$, and matrix loss modulus $E''$, was implemented in a volumetric heat source within the sample, withholding the melting enthalpy during phase change at the start of consolidation. Based on a user-defined weld time, the model generates a cross-sectional temperature gradient through the sample thickness. Using a rule-of-mixtures approach for material properties to account for matrix phase change and volume fractions, it predicts the thermal behavior of the sample throughout consolidation and cooling. Comparison with experimental results for time-input and travel-input trials showed that it can adequately predict temperature profiles to better understand heating phenomena and assist with process control through the weld time and residence time spent above the melting temperature.

It was desirable to determine the time at which the PPS matrix exceeded the melting temperature, and residence time $t_r$ above the melting temperature, to ensure polymer flow and fabric impregnation. In general, higher $t_r$ resulted in better consolidation and lower void content. It was found that $t_{weld}$ values below 1500 ms were insufficient to reach melting temperature, whereas time above 3000 ms led to the lowest average void content (2.43 ± 0.81 %), corresponding to a residence time above 2600 ms.

Overall, the thermal and micro-structural outcomes confirmed the feasibility of the USC process for layered composites made from dry fabric plies and high-temperature thermoplastic films. Each sample was manufactured in less than 6 seconds in a single consolidation step.

### 5.2. Future Work

While current limitations include sample size, future work encompasses further investigation of experimental parameters and improvements to the current model:

- Assessment of maximum thickness and size limits, and effect of post-consolidation (solidification force and time) on sample quality. The current model can be utilized to upscale the process to larger sonotrode sizes and obtain more representative samples for mechanical characterization.
- Model improvements include more accurate cooling phase prediction and implementation of cyclic sinusoidal mechanical behavior. Accuracy of predicted through-the-thickness temperature variation can also be investigated and improved.
- This model can be used to develop the USC process for other polymer matrices and reinforcement types/sequences (unidirectional and woven). Investigation of the effects of weave style/density of dry woven fabric reinforcements on degree of impregnation

and consolidation of USC specimens could provide useful insight on connections to specimen quality.

- Mechanical characterization can be used to support microstructural outcomes identified by void characterization. Mechanical testing can also be used to investigate failure mechanisms (i.e. delamination, matrix debonding) that may be indicators of poor/insufficient consolidation not captured by image analysis.

# APPENDIX A. TIME-TEMPERATURE EXTRAPOLATION

The dynamic mechanical analyzer (DMA) data were shifted onto the *f* = 1 Hz curve. Assuming:

$$E(T, f) = E(T + a(f \rightarrow 1), 1) \qquad (A1)$$

where *E* is the loss or storage modulus, *f* is the frequency, and *a* is the corresponding shift factor. Loss modulus values at room temperature were taken from tests were taken at frequencies of 0.1, 1, 10, and 100 Hz and shifted to the 1 Hz curve using Eqn. (A1). The shift factor *a* for each case was plotted on a semi-log scale versus frequency, and a linear average was used to extrapolate to 20kHz.

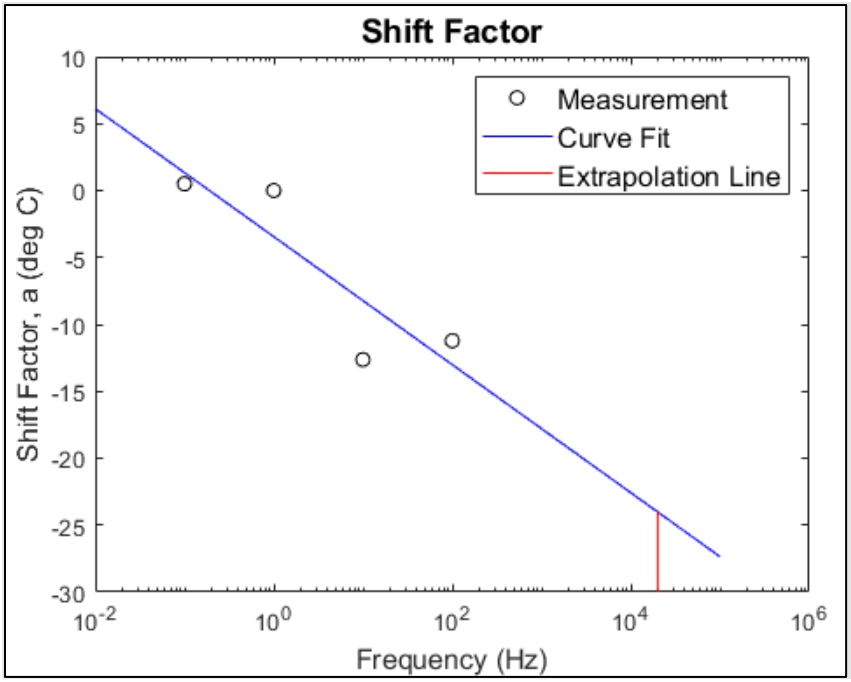


Figure A.1. Linear approximation used to obtain shift factor through plotting on a semi-log scale.

## APPENDIX B. STRAIN AMPLITUDE CALCULATION

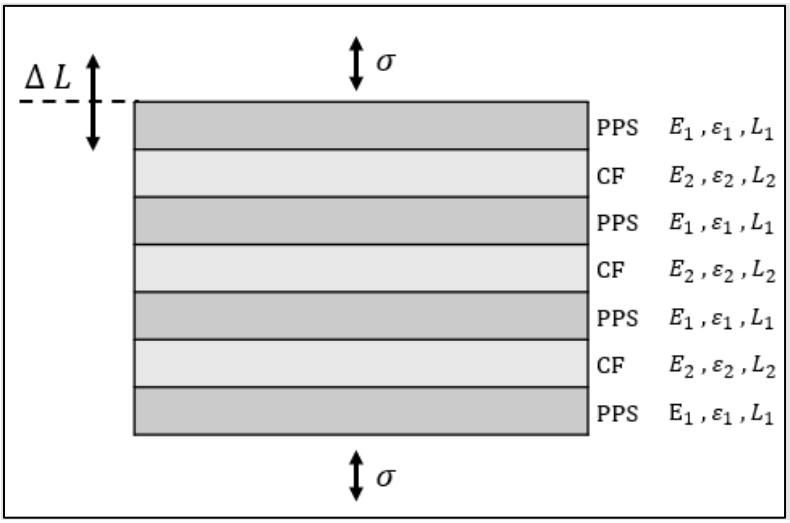


Figure B.1. Material stack with four layers of PPS films and three layers of dry woven CF.

Based on Figure B.1, the stress, $\sigma$, is given by Eq. (B1):

$$\sigma = \varepsilon_1 E_1 = \varepsilon_2 E_2 \qquad (B1)$$

$$\varepsilon_1 = \varepsilon_2 \frac{E_2}{E_1} \qquad (B2)$$

The total displacement, $\Delta L$, is the sum of the individual displacements, such that:

$$\Delta L = 4\varepsilon_1 L_1 + 3\varepsilon_2 L_2 \qquad (B3)$$

Substituting these values and solving for $\varepsilon_2$:

$$\varepsilon_2 = \frac{\Delta L}{4\frac{E_2}{E_1} L_1 + 3L_2} \qquad (B4)$$

The displacement, $\Delta L$, is given by the amplitude of vibration used during welding, which was half the peak-to-peak amplitude of 76.2 $\mu m$. The average strain was then calculated to be:

$$\varepsilon_2 = \varepsilon_0 = \frac{19.05\ \mu m}{4\left(\frac{2.03e6\ Pa}{2.14e9\ Pa}\right)(0.08mm) + 3(0.5\ mm)} = \mathbf{0.0127}$$

# APPENDIX C. INFRARED IMAGING

Thermal images were taken in an early round of experimentation with the aim of obtaining additional thermal information that could be used to validate temperature measurements obtained with thermocouple readings. At this point, the samples were consolidated using identical parameters to the travel-input trials in the main study, except for a higher holding time of 4 seconds.

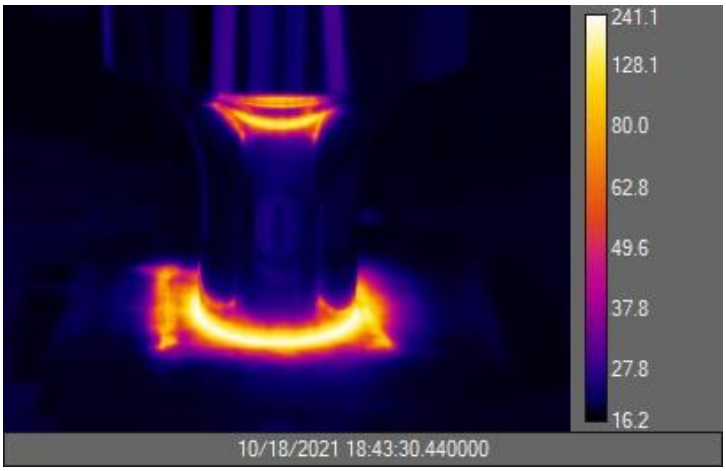


Figure C.1. Thermal image of 0.11mm travel CF/PPS specimen at peak temperature during consolidation.

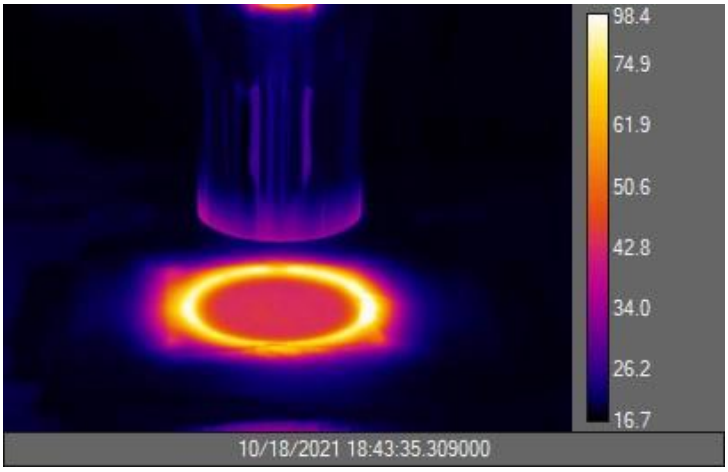


Figure C.2. Thermal image of 0.11mm travel CF/PPS specimen during post-consolidation cooling.

This data can be used to better understand the through-the-thickness temperature gradient of the material. Once the weld cycle is completed and the sonotrode is lifted from the sample, the temperature data obtained from the infrared camera can be used to assess the vertical temperature variation within the specimen at a specific point in time. For each case, times of interest were identified by isolating the frame at which the sonotrode movement stopped in the video footage. The corresponding thermocouple temperature measurements were plotted against top surface temperatures found with IR imaging for comparison in Figure C.3. Difference in measured temperature vs. vertical distance from the top of specimen for CF/PPS samples in cooling phase (after loss of contact with sonotrode).

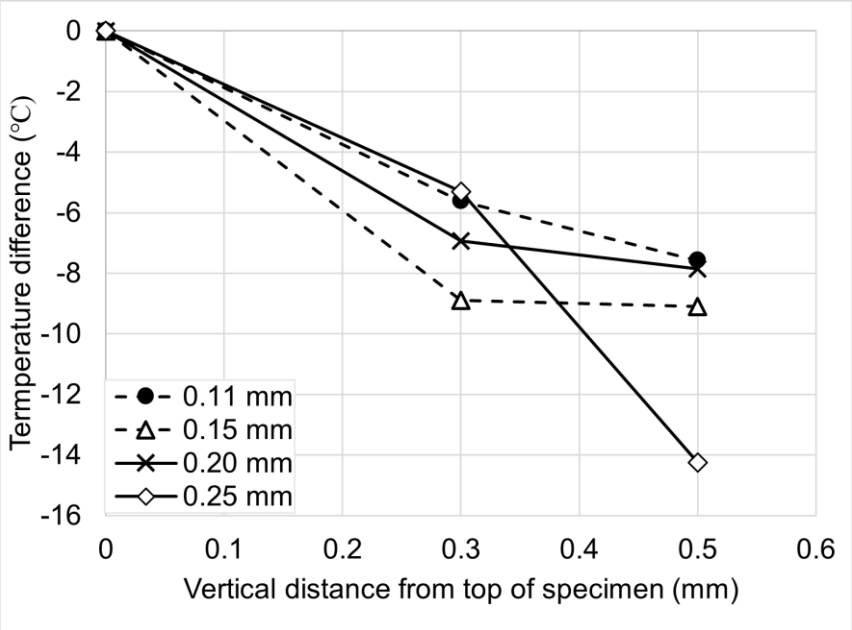


Figure C.3. Difference in measured temperature vs. vertical distance from the top of specimen for CF/PPS samples in cooling phase (after loss of contact with sonotrode).

## APPENDIX D. μCT AND OPTICAL MICROSCOPY

μCT was conducted on the 4 travel-input specimens for void content assessment. Due to technological limitations, Avizo software could not be used to assess void content from a three-dimensional render. Therefore, DICOM slices (as shown in Figures D.1-D.4) from each specimen were used to determine average void content through ImageJ brightness thresholding.

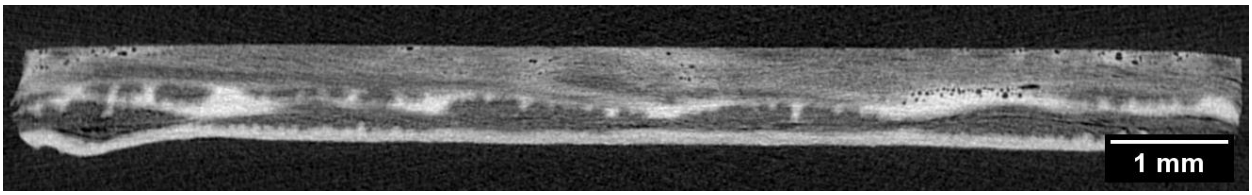


Figure D.1. Representative μCT slice of 0.11 mm CF/PPS specimen.

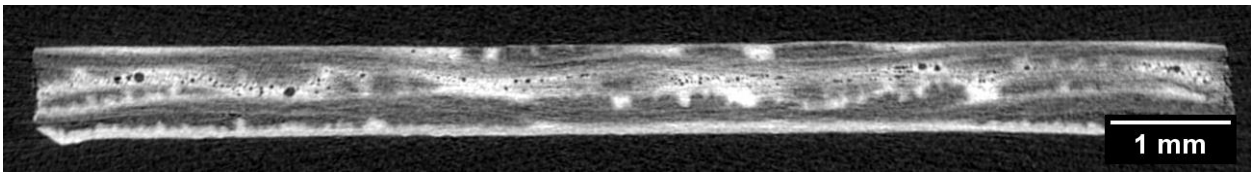


Figure D.2. Representative μCT slice of 0.15 mm CF/PPS specimen.

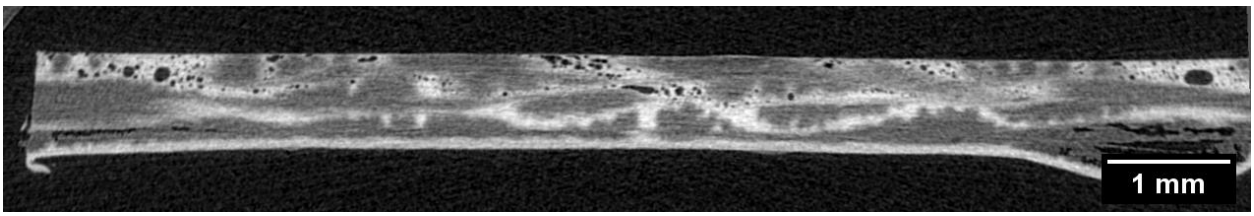


Figure D.3. Representative μCT slice of 0.20 mm CF/PPS specimen.

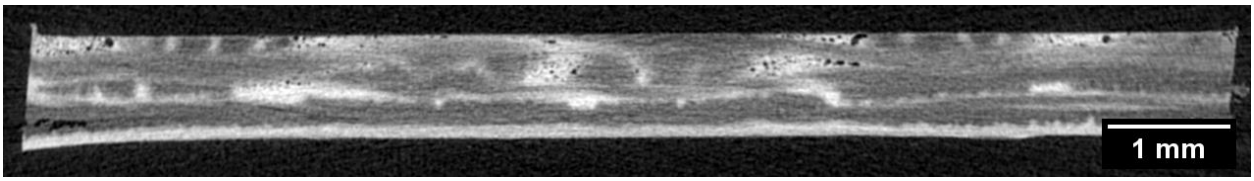


Figure D.4. Representative μCT slice of 0.25 mm CF/PPS specimen.

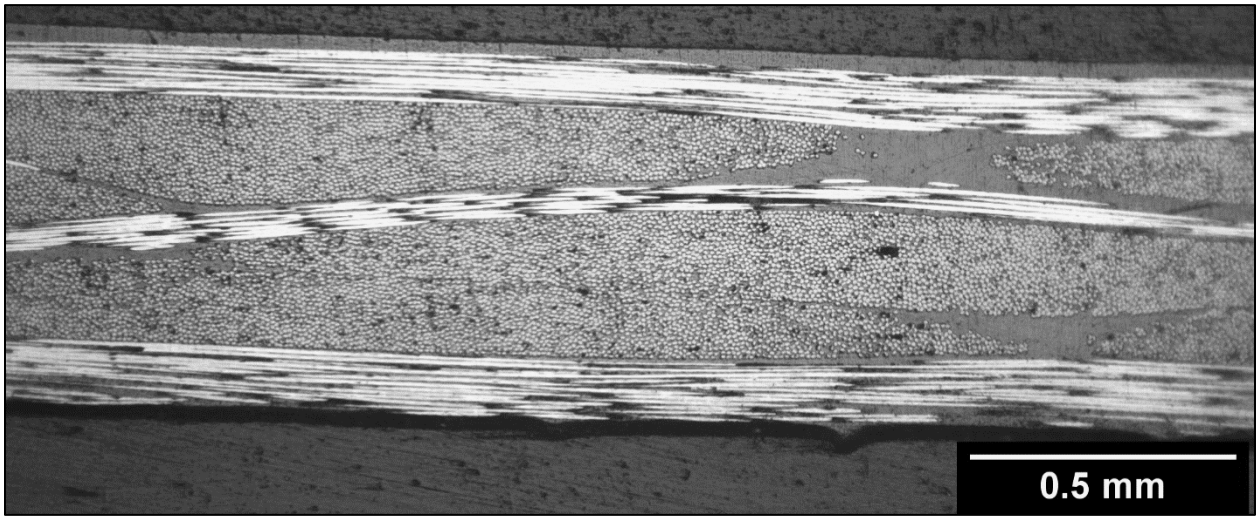


Figure D.5. Representative microscope capture of compression molded CF/PPS specimen at 10x magnitude.

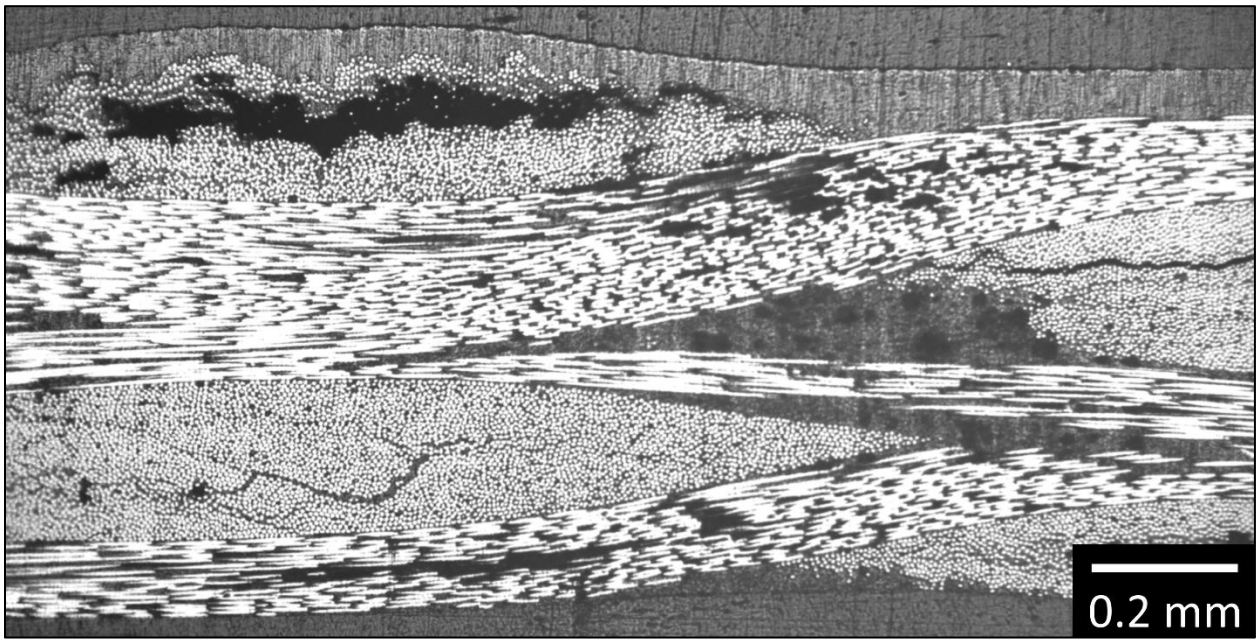


Figure D.6. Representative microscope capture of 0.11 mm travel-input CF/PPS specimen at 10x magnitude.

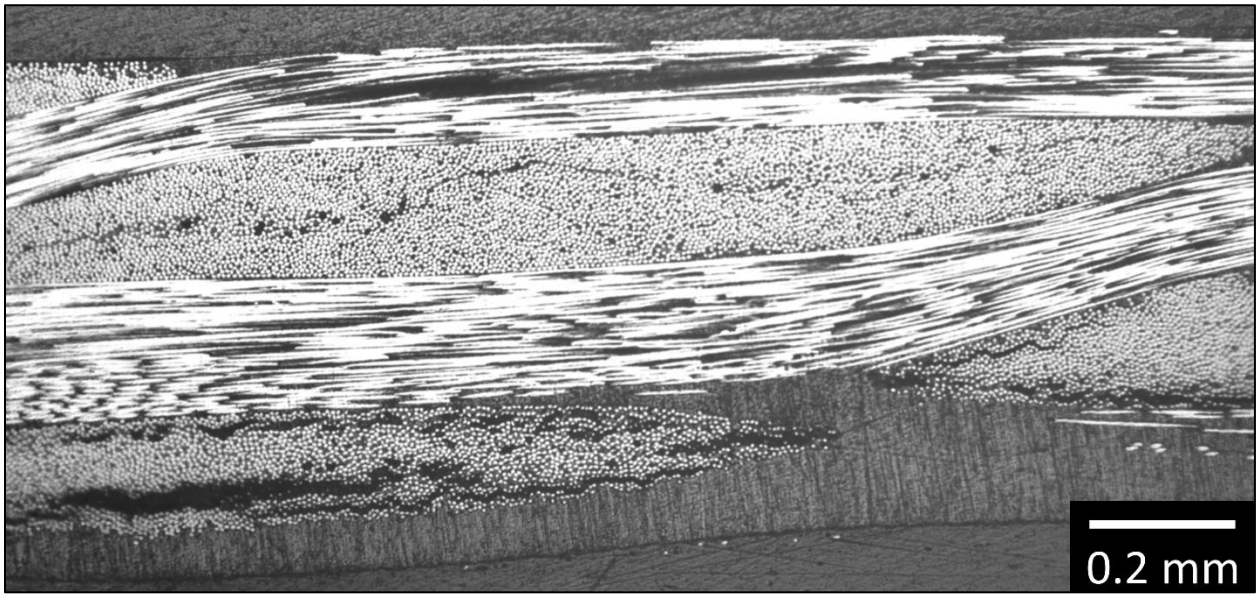


Figure D.7. Representative microscope capture of 0.15 mm travel-input CF/PPS specimen at 10x magnitude.

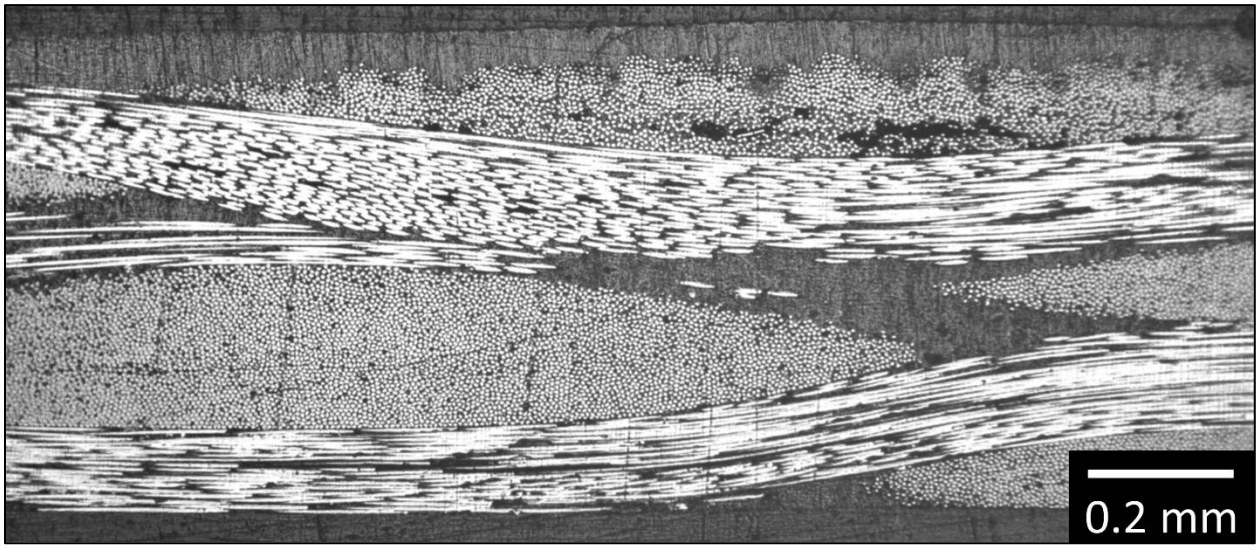


Figure D.8. Representative microscope capture of 0.20 mm travel-input CF/PPS specimen at 10x magnitude.

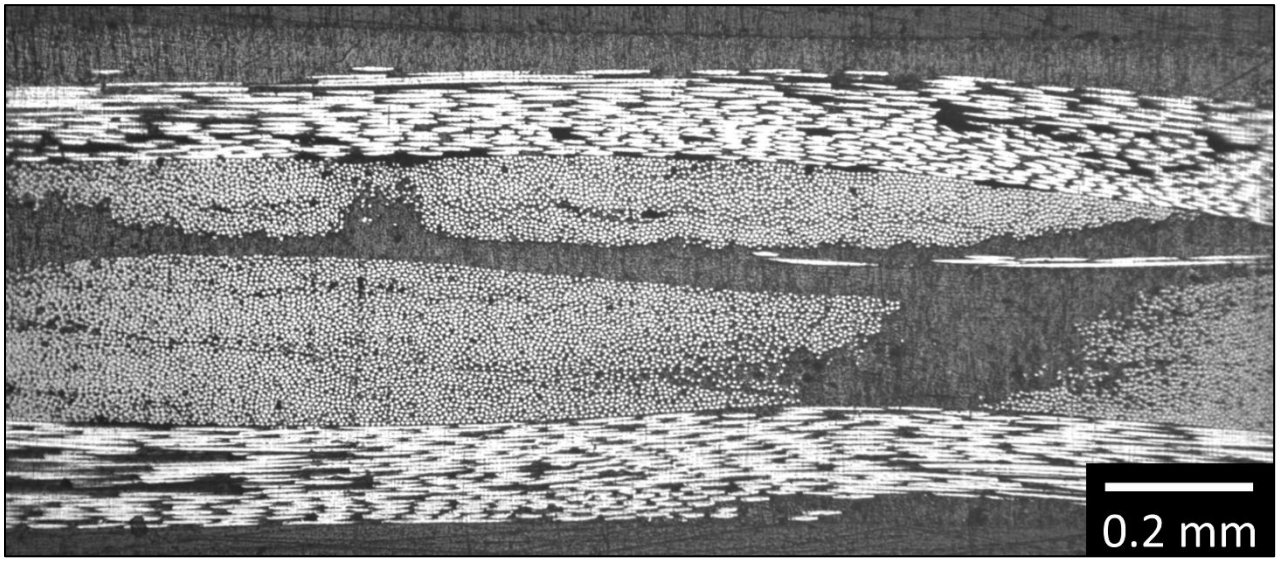


Figure D.9. Representative microscope capture of 0.25mm travel-input CF/PPS specimen at 10x magnitude.

# APPENDIX E. MATLAB CODE

```
clear;clc

%Sample and Welder Dimensions
    hs = 0.01; %height of sonotrode, m
    r = 0.02; %sonotrode radius, m
    hp = 0.01; %height of platform, m
    wp = 0.075; %width of platform, m

    w = 0.05; %overall sample width, m
    t_pps = 0.0762e-3; %thickness of PPS film, m
    t_CF = 0.0005; %thickness of CF ply, m
    t = 4*t_pps+3*t_CF; %overall sample thickness, m
    A = 0.05^2; %overall sample area, m^2

%Welding parameters
    amp = 77.8e-6; %Vibration amplitude, m
    travel = 0.28e-3; %Sonotrode travel, m
    force = 2000; %Consolidation force, N
    fun = 20e3; %Applied frequency, Hz
    T_amb = 20; %Ambient temperature, C
    T0 = T_amb + 273.15; %Ambient temperature, K
    T_con = 273.15; %Convert C to K
    weld_time = 3.250; %duration of applied vibration, seconds
    holding_time = 2; %seconds
    time = weld_time + holding_time ; %overall contact time, seconds
    sim_time = 10; %Overall simulation time, seconds

% Viscoelastic Heating
%Elastic Moduli
    E_pps = 2.53e9; %Pa
    E_CF = 125e9; %Pa

%For Constant Loss Modulus
    omega = 2*pi*fun; %rad/s
    loss_modulus = .02808e9; %Pa, average at 27.4 deg C
    epsilon_0 = (amp/2)/(4*E_pps/E_CF*t_pps + t_CF); %strain amplitude*,
    alpha = .14; %hammer factor
    Q = alpha*(omega*epsilon_0^2*loss_modulus)/2; %Avg power diss. per unit vol, W/m^3

% DSC Nonlinear Regression
%Import DSC data
    dsc = readtable('PPS_Corrected.xlsx','VariableNamingRule','preserve'); %import corrected data
    T = table2array(dsc); %convert spreadsheet to matrix

% Assign vector quantities for temperature and heat flow
    temp = T(:,2) + T_con; %Create vector for temperature, convert to K
    H = T(:,3); %Create vector for heat flow, J/s or W
    Ht = H(length(H)); %Integral over entire curve, J
    [val,k] = max(H);
    Tc = temp(k);
```

```
%Evaluate experimental data
    Xm_data = T(:,4); %Create vector for degree of melting
    for i = 1:length(Xm_data)-1
        dXm_data(i) = (Xm_data(i+1)-Xm_data(i))/(temp(i+1)-temp(i));
    end

% Statistical Approach
%Xm
    d = 9.428; %From curve fitting tool. See PPS_Sigmoidal_Growth.sfit
    kmb = 0.6566; %From curve fitting tool. See PPS_Sigmoidal_Growth.sfit
    peak_check = kmb*d^(d/(1-d));
    Xm = @(t) (1./(1+d.*exp(-kmb.*(t-Tc))).^(1./d)).*(t<=temp(length(temp)))...
        + 1*(t> temp(length(temp)));

% dXm/dT
    syms x
    fun = 1/(1+d*exp(-kmb*(x-Tc)))^(1/d);
    F = diff(fun);
    dXm = matlabFunction(F);
    peak_check = kmb*d^(d/(1-d));

% Melting Heat of PP matrix
    H_dot_m(:,1) = Ht.*dXm(temp); %J
    DSC_Sample_Size = 0.0035; %kg

% Material Properties
% Volume Fraction

    %Calculate Volumes
    V_pps = 4*t_pps*A; %PPS volume, m^3
    V_CF = 3*t_CF*A; %CF volume, m^3
    V = V_pps + V_CF; %Total volume, m^3

    %Calculate Volume Fractions
    Vf_air = 0.5 ; %Volume fraction of air in dry CF (assumed for now), %
    Vf_pps = V_pps/V; %Volume fraction of PPS, %
    Vf_CF = (V_CF/V)*(1-Vf_air); %Volume fraction of CF, %

    %Continuity Check
    V_check = Vf_air + Vf_pps + Vf_CF;

% Thermal Conductivity (W/m-K)
    k_sonotrode_0 = 18; %Titanium
    k_platform = 15; %Stainless steel

    % Individual Thermal Conductivities
    k_pps = 0.30;
    k_CF = 10.5;
    k_air = 0.026;

    % Composite Thermal Conductivities
    k_wet = k_pps*Vf_pps + k_CF*Vf_CF;
    k_dry = k_pps*Vf_pps + k_CF*Vf_CF + k_air*Vf_air;
```

```
%Specific Heat (J/kg-K)
    Cp_sonotrode_0 = 544; %Titanium
    Cp_platform = 502; %Stainless

    % Individual Specific Heats
    Cp_pps = 1000;
    Cp_CF = 777;
    Cp_air = 1005;

    % Composite Specific Heats
    Cp_wet = Cp_pps*Vf_pps + Cp_CF*Vf_CF;
    Cp_dry = Cp_pps*Vf_pps + Cp_CF*Vf_CF + Cp_air*Vf_air;

%Density (kg/m^3)
    rho_sonotrode_0 = 4507; %Titanium
    rho_platform = 7860; %Stainless steel
    rho_air = 1.225; %Air

    %Sample
    rho_CF = 1760;
    rho_pps = 1264;
    rho_pps_am = 1082;

% PDE
thermalmodel = createpde('thermal','transient'); %Create model

% Create representative geometry
    %Create solid objects for each component
    Sonotrode = [3 ; 4 ; -r ; r ; r ; -r; t/2 ; t/2 ; t/2 + hs ; t/2 + hs]; %m, representative
dimensions of sonotrode
    Sample = [3 ; 4 ; -w/2 ; w/2 ; w/2 ; -w/2; -t/2 ; -t/2 ; t/2 ; t/2]; %m, dimensions of sample
    Sample_Contact = [3 ; 4 ; -r ; r ; r ; -r; 0.9*(t/2) ; 0.9*(t/2) ; 1.1*t/2 ; 1.1*t/2]; %m,
dimensions of sample contact area
    Platform = [3 ; 4 ; -wp/2; wp/2 ; wp/2; -wp/2; -t/2 ; -t/2 ; -(t/2 + hp) ; -(t/2 + hp)]; %m,
representative dimensions of weld platform

    %Construct representative geometry
    gd = [Sonotrode,Sample,Sample_Contact,Platform]; %Group all solid objects
    sf = 'Sonotrode+Sample+Sample_Contact+Platform'; %Set formula for solid object grouping
    ns = char('Sonotrode','Sample','Sample_Contact','Platform')'; %Relate columns in gd to
variables in sf
    g = decsg(gd,sf,ns); %Decompose solid objects into minimal regions
    g = geometryFromEdges(thermalmodel,g); %Convert solid object to geometry object
    thermalmodel.Geometry = g; %assign geometry object to thermal model

 %Remove commented code to plot geometry
% figure
% pdegplot(g,'EdgeLabels','on','FaceLabels','on');
% title('Block Geometry With Edge Labels Displayed');

%Generate Mesh
msh = generateMesh(thermalmodel); %create mesh
pdemesh(thermalmodel); %plots mesh over geometry
```

```
%Specify temperature-dependent material properties and heat source
    %Sample Properties

    %Density (kg/m^3)
    rho = @(location,state) rho_CF*Vf_CF + ...
        (1-Vf_CF)*(rho_pps*Xm(state.u) + rho_pps_am*(1-Xm(state.u)));

    %Heat generation term (W/m^3)
    H1 = @(location,state) Q*(state.time <= weld_time); %Viscoelastic heating
    H2 = @(location,state) -rho(location,state)*Ht.*dXm(state.u)/DSC_Sample_Size.*...
        ((Xm(state.u) >= 1e-3)*((state.time <= weld_time) + (state.time > weld_time)*-1));
%enthalpy of fusion
    H = @(location,state) H1(location,state) + H2(location,state)

    %Thermal conductivity (W/m-K)
    k = @(location,state) k_dry*(1-Xm(state.u)) + k_wet*Xm(state.u);

    %Specific heat (J/kg-K)
    cp = @(location,state) Cp_dry*(1-Xm(state.u)) + Cp_wet*Xm(state.u);

    %Change in properties for sonotrode loss of contact
    k_sonotrode = @(location,state) ones(size(location.x))*...
        (k_sonotrode_0.*(state.time <= time) + k_air.*(state.time > time));
    rho_sonotrode = @(location,state) ones(size(location.x))*...
        rho_sonotrode_0.*(state.time <= time) + rho_air.*(state.time > time);
    Cp_sonotrode = @(location,state) ones(size(location.x))*...
        Cp_sonotrode_0.*(state.time <= time) + Cp_air.*(state.time > time);

%Assign material properties
    %Sonotrode
    thermalProperties(thermalmodel,'ThermalConductivity',k_sonotrode,...
                        'MassDensity',rho_sonotrode,'SpecificHeat',Cp_sonotrode,'Face',[2 5]);
    %Sample
    thermalProperties(thermalmodel,'ThermalConductivity',k,...
                        'MassDensity',rho,'SpecificHeat',cp,'Face',[1 4]);
    %Platform
    thermalProperties(thermalmodel,'ThermalConductivity',k_platform,...
                        'MassDensity',rho_platform,'SpecificHeat',Cp_platform,'Face',3);

%Specify ICs, BCs, and heat sources
internalHeatSource(thermalmodel,H,'Face',[4 5]);
thermalIC(thermalmodel,T0); %set initial temp for all surfaces
% thermalBC(thermalmodel,'Temperature',T0,'Edge',[1 6 7 5]);
% thermalBC(thermalmodel,'Edge',[1 2 3 4 5 6 7 9 10 12 14 15 17],...
%             'ConvectionCoefficient',5,'AmbientTemperature',293.15);

%Specify timestep size
nframes = sim_time*20; %set animation fps
tlist = linspace(0,sim_time,nframes); %populate time vector

thermalmodel.SolverOptions.ReportStatistics = 'on';
results = solve(thermalmodel,tlist); %solves the PDE
```

```
%Extract temperature results
T = results.Temperature - T_con; %Converts temp from K to C

%Specify min and max for colormap legend
Tmin = min(min(T)); Tmax = max(max(T));

%Specify Temperature Nodes
X = [0 0 ];
Y = [-t/2 t/2] ;

%Extract node temperatures and plot vs time
figure
for ii = 1:length(X)
    Pointdata(:,ii) = interpolateTemperature(results,X(ii),Y(ii),1:length(tlist)) - T_con;
    plot(tlist,Pointdata(:,ii))
    hold on
end
title('Theoretical Thermocouple Node Temperature vs Time','fontsize',12)
xlabel('Time (s)','fontsize',12)
ylabel('Temperature (C)','fontsize',12)
legend('Node 1','Node 2','Node 3','fontsize',12)

%Write to Excel File
Tabulate = [tlist' Pointdata];
xlswrite('Theoretical_Temp325Oms.xlsx',Tabulate)

% Create Video File
% set(gca,'nextplot','replacechildren');
% v = VideoWriter('TempMap.mp4','MPEG-4');
% v.Quality = 95;
%
% Plot animated figure and save frames to video file
% h = figure;
% open(v);
% for i = 1:numel(tlist)
%     pdeplot(thermalmodel,'XYData',T(:,i),'ColorMap','jet')
%     title(['Temperature (C) at Time ' num2str(tlist(i))] );
%     caxis([Tmin, Tmax])
%     xlim([-9*w/16 9*w/16])
%     ylim([-t t])
%     axis equal
%     M = getframe(gcf);
%     writeVideo(v,M)
% end
% close(v);
```

## REFERENCES


[1] A. Yousefpour, M. Hojjati, and J.-P. Immarigeon, "Fusion Bonding/Welding of Thermoplastic Composites," *Journal of Thermoplastic Composite Materials,* vol. 17, no. 4, pp. 303-341, July 1, 2004 2004, doi: 10.1177/0892705704045187.

[2] S. Williams and G. Palardy, "Ultrasonic consolidation of dry carbon fiber and polyphenylene sulfide film," presented at the SAMPE Virtual Series, July 20, 2020.

[3] H. Ning, (Thermoplastic Composites: Principles and Applications). De Gruyter, 2021.

[4] M. Biron, "Thermoplastics and thermoplastic composites," (in English), 2018. [Online]. Available: https://search.ebscohost.com/login.aspx?direct=true&scope=site&db=nlebk&db=nlabk&AN=1655720.

[5] P. Krawczak and A. Maffezzoli, "Advanced thermoplastic composites and manufacturing processes," *Frontiers in Materials,* vol. 7, p. 166, 07/09 2020, doi: 10.3389/fmats.2020.00166.

[6] J. Mack and R. Schledjewski, "7 - Filament winding process in thermoplastics," in *Manufacturing Techniques for Polymer Matrix Composites (PMCs)*, S. G. Advani and K.-T. Hsiao Eds.: Woodhead Publishing, 2012, pp. 182-208.

[7] Y. D. Boon, S. C. Joshi, and S. K. Bhudolia, "Review: Filament Winding and Automated Fiber Placement with In Situ Consolidation for Fiber Reinforced Thermoplastic Polymer Composites," *Polymers,* vol. 13, no. 12, p. 1951, 2021. [Online]. Available: https://www.mdpi.com/2073-4360/13/12/1951.

[8] J. L. Hull, "Compression and Transfer Molding," in *SPI Plastics Engineering Handbook of the Society of the Plastics Industry, Inc.*, M. L. Berins Ed. Boston, MA: Springer US, 1991, pp. 251-288.

[9] S. M. Sapuan, "Chapter 3 - Composite Materials," in *Composite Materials*, S. M. Sapuan Ed. Boston: Butterworth-Heinemann, 2017, pp. 57-93.

[10] N. Mahmud, R. Lin, and K. Jayaraman, "Flammability, thermal and dynamic mechanical properties of bamboo-glass hybrid composites," *Journal of*

*Thermoplastic Composite Materials,* vol. 29, 12/14 2014, doi: 10.1177/0892705714563118.

[11] T. Slange, L. L. Warnet, W. Grouve, and R. Akkerman, *Influence of preconsolidation on consolidation quality after stamp forming of C/PEEK composites*. 2016, p. 170022.

[12] N. I. f. A. R. Society of Automotive Engineers, "Composite materials handbook. Volume 3, Volume 3," (in English), 2012. [Online]. Available: http://app.knovel.com/hotlink/toc/id:kpCMHVPM1E/composite-materials-handbook.

[13] R. A. Brooks *et al.*, "A review on stamp forming of continuous fibre-reinforced thermoplastics," *International Journal of Lightweight Materials and Manufacture,* vol. 5, no. 3, pp. 411-430, 2022/09/01/ 2022, doi: https://doi.org/10.1016/j.ijlmm.2022.05.001.

[14] I. I. Rubin, "Injection Molding of Thermoplastics," in *SPI Plastics Engineering Handbook of the Society of the Plastics Industry, Inc.*, M. L. Berins Ed. Boston, MA: Springer US, 1991, pp. 133-178.

[15] A. M. Sastry, "2.17 - Impregnation and Consolidation Phenomena," in *Comprehensive Composite Materials*, A. Kelly and C. Zweben Eds. Oxford: Pergamon, 2000, pp. 609-622.

[16] I. Fernández, F. Blas, and M. Frövel, "Autoclave forming of thermoplastic composite parts," *Journal of Materials Processing Technology,* vol. 143-144, pp. 266-269, 2003/12/20/ 2003, doi: https://doi.org/10.1016/S0924-0136(03)00309-1.

[17] A. Brasington, C. Sacco, J. Halbritter, R. Wehbe, and R. Harik, "Automated fiber placement: A review of history, current technologies, and future paths forward," *Composites Part C: Open Access,* vol. 6, p. 100182, 2021/10/01/ 2021, doi: https://doi.org/10.1016/j.jcomc.2021.100182.

[18] K. Kozaczuk, "Automated fiber placement systems overview," *Transactions of the Institute of Aviation,* vol. 245, pp. 52-59, 2016.

[19] H. Mason. "Mikrosam to supply GKN Fokker with AFP, consolidation equipment for thermoplastic composites." CompositesWorld.

https://www.compositesworld.com/news/mikrosam-to-supply-gkn-fokker-with-afp-consolidation-equipment-for-thermoplastic-composites- (accessed.

[20] N. Krajangsawasdi, L. G. Blok, I. Hamerton, M. L. Longana, B. K. S. Woods, and D. S. Ivanov, "Fused Deposition Modelling of Fibre Reinforced Polymer Composites: A Parametric Review," *Journal of Composites Science,* vol. 5, no. 1, p. 29, 2021. [Online]. Available: https://www.mdpi.com/2504-477X/5/1/29.

[21] A. N. Dickson, H. M. Abourayana, and D. P. Dowling, "3D Printing of Fibre-Reinforced Thermoplastic Composites Using Fused Filament Fabrication—A Review," *Polymers,* vol. 12, no. 10, p. 2188, 2020. [Online]. Available: https://www.mdpi.com/2073-4360/12/10/2188.

[22] "Fiber™." Desktop Metal. https://www.desktopmetal.com/products/fiber (accessed.

[23] "Technology: AQUA System." AREVO. https://arevo.com/products?lang=en (accessed.

[24] S. Shimizu, H. T. Fujii, Y. S. Sato, H. Kokawa, M. R. Sriraman, and S. S. Babu, "Mechanism of weld formation during very-high-power ultrasonic additive manufacturing of Al alloy 6061," *Acta Materialia,* vol. 74, pp. 234-243, 2014/08/01/ 2014, doi: https://doi.org/10.1016/j.actamat.2014.04.043.

[25] R. J. Friel and R. A. Harris, "Ultrasonic Additive Manufacturing – A Hybrid Production Process for Novel Functional Products," *Procedia CIRP,* vol. 6, pp. 35-40, 2013/01/01/ 2013, doi: https://doi.org/10.1016/j.procir.2013.03.004.

[26] F. Lionetto, R. Dell'Anna, F. Montagna, and A. Maffezzoli, "Ultrasonic Assisted Consolidation of Commingled Thermoplastic/Glass Fiber Rovings," (in English), *Frontiers in Materials,* Original Research vol. 2, no. 32, 2015-April-21 2015, doi: 10.3389/fmats.2015.00032.

[27] F. Lionetto, R. Dell'Anna, F. Montagna, and A. Maffezzoli, "Modeling of continuous ultrasonic impregnation and consolidation of thermoplastic matrix composites," *Composites Part A: Applied Science and Manufacturing,* vol. 82, pp. 119-129, 2016/03/01/ 2016, doi: https://doi.org/10.1016/j.compositesa.2015.12.004.

[28] R. H. Rizzolo and D. F. Walczyk, "Ultrasonic consolidation of thermoplastic composite prepreg for automated fiber placement," *Journal of Thermoplastic*

*Composite Materials,* vol. 29, no. 11, pp. 1480-1497, 2016/11/01 2015, doi: 10.1177/0892705714565705.

[29] A. Gomer, W. Zou, N. Grigat, J. Sackmann, and W. Schomburg, "Fabrication of Fiber Reinforced Plastics by Ultrasonic Welding," *Journal of Composites Science,* vol. 2, no. 3, p. 56, 2018. [Online]. Available: http://www.mdpi.com/2504-477X/2/3/56.

[30] Q. Zhi, X.-R. Tan, L. Lu, L.-Y. Chen, J.-C. Li, and Z.-X. Liu, "Decomposition of ultrasonically welded carbon fiber/polyamide 66 and its effect on weld quality," *Welding in the World,* vol. 61, no. 5, pp. 1017-1028, 2017/09/01 2017, doi: 10.1007/s40194-017-0482-5.

[31] I. F. Villegas, "In situ monitoring of ultrasonic welding of thermoplastic composites through power and displacement data," *Journal of Thermoplastic Composite Materials,* vol. 28, no. 1, pp. 66-85, 2015, doi: 10.1177/0892705712475015.

[32] S. K. Bhudolia, G. Gohel, K. F. Leong, and R. J. Barsotti, "Investigation on Ultrasonic Welding Attributes of Novel Carbon/Elium® Composites," *Materials,* vol. 13, no. 5, p. 1117, 2020. [Online]. Available: https://www.mdpi.com/1996-1944/13/5/1117.

[33] B. Jongbloed, J. Teuwen, G. Palardy, I. Fernandez Villegas, and R. Benedictus, "Continuous ultrasonic welding of thermoplastic composites: Enhancing the weld uniformity by changing the energy director," *Journal of Composite Materials,* vol. 54, no. 15, pp. 2023-2035, 2020, doi: 10.1177/0021998319890405.

[34] M. Engelschall, L. Larsen, F. Fischer, and M. Kupke, "Robot-based Continuous Ultrasonic Welding for Automated Production of Aerospace Structures," in *SAMPE Europe*, Nantes, France, 2019.

[35] K. Yassin and M. Hojjati, "Processing of thermoplastic matrix composites through automated fiber placement and tape laying methods: A review," *Journal of Thermoplastic Composite Materials,* vol. 31, no. 12, pp. 1676-1725, 2018/12/01 2017, doi: 10.1177/0892705717738305.

[36] R. Dell'Anna, F. Lionetto, F. Montagna, and A. Maffezzoli, "Lay-Up and Consolidation of a Composite Pipe by In Situ Ultrasonic Welding of a Thermoplastic Matrix Composite Tape," (in eng), *Materials (Basel),* vol. 11, no. 5, p. 786, 2018, doi: 10.3390/ma11050786.

[37] A. Levy, S. Le Corre, and I. Fernandez Villegas, "Modeling of the heating phenomena in ultrasonic welding of thermoplastic composites with flat energy directors," *Journal of Materials Processing Technology,* vol. 214, no. 7, pp. 1361-1371, 2014/07/01/ 2014, doi: https://doi.org/10.1016/j.jmatprotec.2014.02.009.

[38] Y. Yang, Z. Liu, Y. Wang, and Y. Li, "Numerical Study of Contact Behavior and Temperature Characterization in Ultrasonic Welding of CF/PA66," *Polymers,* vol. 14, no. 4, p. 683, 2022. [Online]. Available: https://www.mdpi.com/2073-4360/14/4/683.

[39] M. Mehdikhani, L. Gorbatikh, I. Verpoest, and S. V. Lomov, "Voids in fiber-reinforced polymer composites: A review on their formation, characteristics, and effects on mechanical performance," *Journal of Composite Materials,* vol. 53, no. 12, pp. 1579-1669, 2019, doi: 10.1177/0021998318772152.

[40] A. Benatar and Z. Cheng, "Ultrasonic welding of thermoplastics in the far-field," *Polymer Engineering & Science,* vol. 29, no. 23, pp. 1699-1704, 1989, doi: https://doi.org/10.1002/pen.760292312.

[41] I. F. Villegas, "Strength development versus process data in ultrasonic welding of thermoplastic composites with flat energy directors and its application to the definition of optimum processing parameters," *Composites Part A: Applied Science and Manufacturing,* vol. 65, pp. 27-37, 10// 2014, doi: http://dx.doi.org/10.1016/j.compositesa.2014.05.019.

[42] C. B. G. Brito, J. Teuwen, C. A. Dransfeld, and I. F. Villegas, "The effects of misaligned adherends on static ultrasonic welding of thermoplastic composites," *Composites Part A: Applied Science and Manufacturing,* vol. 155, p. 106810, 2022/04/01/ 2022, doi: https://doi.org/10.1016/j.compositesa.2022.106810.

[43] N. Tateishi, T. H. North, and R. T. Woodhams, "Ultrasonic welding using tie-layer materials. part I: Analysis of process operation," *Polymer Engineering & Science,* vol. 32, no. 9, pp. 600-611, 1992, doi: https://doi.org/10.1002/pen.760320906.

[44] A. Greco and A. Maffezzoli, "Statistical and kinetic approaches for linear low-density polyethylene melting modeling," *Journal of Applied Polymer Science,* vol. 89, no. 2, pp. 289-295, 2003, doi: https://doi.org/10.1002/app.12079.

[45] A. N. Tsoularis and J. Wallace, "Analysis of Logistic Growth Models," *Mathematical biosciences,* vol. 179, pp. 21-55, 07/01 2002, doi: 10.1016/S0025-5564(02)00096-2.

[46] G. A. F. Seber and C. J. Wild, *Nonlinear Regression*. Nashville, TN: John Wiley & Sons, 1989, p. 790.

[47] L. Cao, P.-J. Shi, L. Li, and G. Chen, "A New Flexible Sigmoidal Growth Model," *Symmetry,* vol. 11, no. 2, p. 204, 2019. [Online]. Available: https://www.mdpi.com/2073-8994/11/2/204.

[48] M. Roylance, J. Player, W. Zukas, and D. Roylance, "Modeling of ultrasonic processing," *Journal of Applied Polymer Science,* vol. 93, no. 4, pp. 1609-1615, 2004, doi: 10.1002/app.20595.

[49] D. Hoskins and G. Palardy, "High-speed consolidation and repair of carbon fiber/epoxy laminates through ultrasonic vibrations: A feasibility study," *Journal of Composite Materials,* vol. 54, no. 20, pp. 2707-2721, 2020, doi: 10.1177/0021998320903097.

## VITA

Madeline Kirby was born and raised in Plaquemine, Louisiana. After graduating high school from the Iberville Math, Science, and Arts Academy West, she moved to Baton Rouge, Louisiana where she completed her Bachelor of Science in Mechanical Engineering at Louisiana State University (LSU) in May of 2022. In her last year of undergraduate study, she enrolled in the Accelerated Master of Science in Mechanical Engineering (MSME) program at LSU and began graduate research and coursework. After 1.5 years as a full-time graduate student, she plans to earn her MSME in August of 2022. She plans to pursue a career as an aerospace instrumentation analysis engineer upon completion of her degree.